

1 **A fifteen year record of CO emissions constrained by MOPITT CO**  
2 **observations**

4 Zhe Jiang<sup>1,2</sup>, John R. Worden<sup>1</sup>, Helen Worden<sup>2</sup>, Merritt Deeter<sup>2</sup>, Dylan B. A. Jones<sup>3</sup>, Avelino F.  
5 Arellano<sup>4</sup>, Daven K. Henze<sup>5</sup>

8 <sup>1</sup>Jet Propulsion Laboratory, California Institute of Technology, Pasadena, CA, USA

9 <sup>2</sup>National Center for Atmospheric Research, Boulder, CO, USA

10 <sup>3</sup>Department of Physics, University of Toronto, Toronto, ON, Canada

11 <sup>4</sup>Department of Hydrology and Atmospheric Sciences, University of Arizona, Tucson, AZ, USA

12 <sup>5</sup>Department of Mechanical Engineering, University of Colorado, Boulder, CO, USA

13

14

15

16

17

18

19

20

21

22

23

24

25

26

27

28

29 **Abstract**

30 Long-term measurements from satellites and surface stations have demonstrated a  
31 decreasing trend of tropospheric carbon monoxide (CO) in the Northern Hemisphere over the past  
32 decade. Likely explanations for this decrease include changes in anthropogenic, fires, and/or  
33 biogenic emissions or changes in the primary chemical sink hydroxyl radical (OH). Using  
34 remotely sensed CO measurements from the Measurement of Pollution in the Troposphere  
35 (MOPITT) satellite instrument, in-situ methyl chloroform (MCF) measurements from World Data  
36 Centre for Greenhouse Gases (WDCGG), and the adjoint of the GEOS-Chem model, we estimate  
37 the change in global CO emissions from 2001-2015. We show that the loss rate of MCF varies by  
38 0.2% in the past 15 years, indicating that changes in global OH distributions do not explain the  
39 recent decrease in CO. Our two-step inversion approach for estimating CO emissions is intended  
40 to mitigate the effect of bias errors in the MOPITT data as well as model errors in transport and  
41 chemistry, which are the primary uncertainties when quantifying CO emissions using these  
42 remotely sensed data. Our results confirm that the decreasing trend of tropospheric CO in the  
43 Northern Hemisphere is due to decreasing CO emissions from anthropogenic and biomass burning  
44 sources. In particular, we find decreasing CO emissions from the United States and China in the  
45 past 15 years, unchanged anthropogenic CO emissions from Europe since 2008. We find  
46 decreasing trends of biomass burning CO emissions from boreal North America, boreal Asia and  
47 South America, but little change over Africa. In contrast to prior results we find a positive trend in  
48 CO emissions is likely for India and southeast Asia.

49

50 **1. Introduction**

51 Tropospheric CO is a product of incomplete combustion and a byproduct of the oxidation

52 of hydrocarbons. It plays a key role in atmospheric chemistry because it is the main sink for OH,  
53 and an important precursor for tropospheric ozone ( $O_3$ ). Recent studies demonstrated significant  
54 change in tropospheric CO abundance in the past decade. Using Atmospheric Infrared Sounder  
55 (AIRS) CO measurements, Warner et al. (2013) indicated that Northern Hemispheric CO mixing  
56 ratio decreased by 1.28 ppb/year in the period of 2003-2012. Worden et al. (2013) demonstrated  
57 Northern Hemispheric CO column measurements from MOPITT show a decrease of ~0.92%/year  
58 in the period of 2000-2011. Using observations from Mt. Bachelor Observatory, Gratz et al. (2015)  
59 also show a negative trend of CO concentration by 1.9%/year in the period of 2004-2013.  
60 However, the reason for the large variation of tropospheric CO abundance is still unclear; for  
61 example, Strode et al. (2016) found decreases in modeled CO abundance over North America and  
62 Europe, but increases over China, based on bottom-up emissions.

63 There is currently much effort focused on accurately quantifying emissions of CO. For  
64 fossil fuels and biofuels, energy consumption statistics and emission factors are usually used to  
65 construct the emission inventories (e.g. Streets et al. 2006; Ohara et al. 2007; Zhang et al. 2009;  
66 Zhao et al. 2012). Biomass burning emissions are commonly calculated as the product of burned  
67 area, fuel loads, combustion completeness and emission factors (e.g. van der Werf et al. 2006,  
68 2010; van Leeuwen and van der Werf 2011). Because of the large uncertainties in the emission  
69 inventories, space-based remotely sensed measurements and surface/aircraft in-situ observations  
70 have been assimilated to provide “top-down” constraints on CO emissions (e.g., Arellano et al.,  
71 2006; Chevallier et al. 2009; Jones et al., 2009; Kopacz et al., 2010; Jiang et al., 2011; Fortems-  
72 Cheiney et al. 2011; Hooghiemstra et al. 2012; Miyazaki et al. 2015). In a recent study, Yin et al.  
73 (2015) constrained global CO emissions for the period 2002-2011 to investigate the possible  
74 reasons for the decreasing CO abundance in the Northern Hemisphere. Using MOPITT column

75 data (version V6J) over the whole globe, Yin et al. (2015) indicate that the negative trend in the  
76 Northern Hemisphere is driven by decreasing anthropogenic emissions from North America,  
77 Europe and China.

78 The major sink of tropospheric CO is OH. Because of its high variability and short lifetime  
79 (about one second), it is difficult to assess the spatial and temporal variation of global OH through  
80 direct measurements (Spivakovskiy et al. 2000; Lelieveld et al. 2004). Alternatively, Montzka et  
81 al. (2011) demonstrated small interannual variability of global OH for the period 1997-2007 by  
82 using the loss rate of MCF as a proxy. The measurements of MCF are assimilated in recent CO  
83 inversion studies to provide updated OH (e.g. Fortems-Cheiney et al. 2011, 2012; Yin et al. 2015),  
84 but the estimates are adversely affected by the sparse distribution of measurements.

85 The objective of this work is to investigate the dominant reasons for the decreasing CO  
86 trend in the Northern Hemisphere, and to provide updated CO emission estimates for model studies.  
87 Using methods and results from our prior work, our approach for estimating emissions is intended  
88 to reduce the effects of model errors of transport and chemistry, as well as bias errors in the data,  
89 on our conclusions about CO emissions; these are the primary uncertainties that affect CO  
90 emissions estimates. For example, bias errors as a function of latitude in MOPITT data can have a  
91 substantial impact on emissions estimates (Deeter et al., 2014). Model errors of transport and  
92 chemistry will have variable and substantial effects on CO emissions in different parts of the globe  
93 due to seasonal and latitudinal variations in convection, advection, and boundary layer height  
94 (Jiang et al., 2013, 2015a, 2015b).

95 In order to reduce the influences from these measurement and model transport systematic  
96 errors, we performed a two-step inversion by combining sequential Kalman Filter (Jiang et al.  
97 2013, 2015a, 2015b) with four-dimensional variational (4D-Var) assimilation (Henze et al. 2007)

98 in this work, using the GEOS-Chem model. Instead of optimizing the CO concentrations and  
99 emissions simultaneously (e.g. Fortems-Cheiney et al. 2011, 2012; Yin et al. 2015), our first step,  
100 the sequential Kalman Filter, modifies the atmospheric CO concentration directly to provide low  
101 bias initial (monthly) and boundary (hourly) conditions, whereas the second step (4D-Var)  
102 constrains CO emissions assuming perfect initial and boundary conditions. We also apply bias  
103 corrections to MOPITT and compare the surface CO concentrations obtained by constraining the  
104 model with either MOPITT profile, total column, or lower troposphere data to test which data type  
105 provides the most accurate comparison with independent surface in-situ measurements.

106 This paper is organized as follows: in Section 2 we describe the MOPITT instruments and  
107 the GEOS-Chem model used in this work. In Section 3 we outline the inverse method. We then  
108 investigate the long-term variations of global tropospheric OH and CO emissions in Section 4, and  
109 we discuss the changes in tropospheric CO, and the contributions from emissions and  
110 meteorological conditions. Our conclusions follow in Section 5.

## 111 **2. Observations and Model**

### 112 **2.1. MOPITT**

113 The MOPITT instrument was launched on December 18, 1999 on the NASA/Terra  
114 spacecraft. The satellite is in a sun-synchronous polar orbit of 705 km and crosses the equator at  
115 10:30 local time. The instrument makes measurements in a 612 km cross-track scan with a  
116 footprint of 22 km x 22 km, and provides global coverage every three days. The MOPITT data  
117 used here were obtained from the joint (J) retrieval (V6J) of CO from TIR (4.7 $\mu$ m) and NIR (2.3 $\mu$ m)  
118 radiances using an optimal estimation approach (Worden et al., 2010; Deeter et al., 2011). The  
119 retrieved volume mixing ratios (VMR) are reported as layer averages of 10 pressure levels (surface,  
120 900, 800, 700, 600, 500, 400, 300, 200 and 100 hPa). The relationship between the retrieved CO

121 profile and the true atmospheric state can be described as:

122 
$$\hat{z} = z_a + A(z - z_a) + G\epsilon \quad (1)$$

123 where  $z_a$  is the MOPITT a priori CO profile,  $z$  is the true atmospheric state,  $G\epsilon$  describes the  
124 retrieval error, and  $A = \partial\hat{z}/\partial z$  is the MOPITT averaging kernel matrix, which gives the sensitivity  
125 of the retrieval to the actual CO in the atmosphere. The MOPITT V6 data have been evaluated by  
126 Deeter et al. (2014) using aircraft measurements from HIAPER Pole-to-Pole Observations (HIPPO)  
127 and the National Oceanic and Atmospheric Administration (NOAA). For the TIR/NIR multi-  
128 spectral retrievals, they found negative bias drift (-1.27%/year) at lower troposphere (800 hPa),  
129 and positive bias drift (1.64%/year) at upper troposphere (200 hPa). The bias drift in the total  
130 column is negligible (0.15%/year). Following our previous studies (Jiang et al. 2013; 2015a;  
131 2015b), we reject MOPITT data with CO column amounts less than  $5 \times 10^{17}$  molec/cm<sup>2</sup> and with  
132 low cloud observations. The threshold of  $5 \times 10^{17}$  molec/cm<sup>2</sup> was selected to prevent unrealistically  
133 low CO columns from adversely impacting the inversion analyses. Since the NIR radiances  
134 measure reflected solar radiation, only daytime data are considered here.

135 Figure 1 shows the comparison between MOPITT CO retrievals and HIPPO aircraft  
136 measurements. The aircraft measurements are smoothed with MOPITT averaging kernels. The  
137 comparison demonstrates a negative bias of MOPITT CO retrievals in the tropics and a positive  
138 bias at the middle latitudes in the lower troposphere. Opposite bias is observed in the upper  
139 troposphere. Similar latitude dependent biases in remote sensing retrievals have been revealed for  
140 methane (CH<sub>4</sub>) observations from Scanning Imaging Absorption Spectrometer for Atmospheric  
141 Chartography (SCIAMACHY, Bergamaschi et al. 2007, 2009; Meirink et al. 2008), Greenhouse  
142 Gases Observing Satellite (GOSAT, Turner et al. 2015), and CO observation from MOPITT  
143 (version 4, Hooghiemstra et al. 2012). Similar to previous studies, we reduce the adverse effect of

144 the latitude dependent bias by applying latitude dependent correction factors to MOPITT CO  
145 retrievals, based on the black solid line in Figure 1, which represents a 4-order polynomial curve  
146 fitting (in a least-squares sense) for all data points. It should be noted that we are only correcting  
147 for a time-invariant latitudinal and vertical dependence of MOPITT CO bias. Seasonal and  
148 interannual variations of MOPITT retrieval biases are not corrected due to the limited spatial  
149 sampling of in situ data available for determining retrieval bias changes over the MOPITT data  
150 record. (Deeter et al., 2014). These remaining bias drifts have implications for interpreting the CO  
151 emissions trends derived from total column vs. profile or lower tropospheric profile.

152 **2.2. GEOS-Chem**

153 The GEOS-Chem global chemical transport model (CTM) [[www.geos-chem.org](http://www.geos-chem.org)] is driven  
154 by assimilated meteorological fields from the NASA Goddard Earth Observing System (GEOS-5)  
155 at the Global Modeling and data Assimilation Office. For the simulations in this work, various  
156 versions of GEOS meteorological fields are used, including GEOS-4 (2000-2003), GEOS-5 (2004-  
157 2012) and GEOS-FP (2013-2015). We use version v35j of the GEOS-Chem adjoint, which is based  
158 on v8-02-01 of the forward GEOS-Chem model, with relevant updates through v9-02-01. Our  
159 analysis is conducted at a horizontal resolution of  $4^{\circ} \times 5^{\circ}$  with 47 vertical levels and employs the  
160 CO-only simulation in GEOS-Chem, which uses archived monthly OH fields from the full  
161 chemistry simulation. The OH fields used in this work are from GEOS-Chem version v5-07-08,  
162 with a global annual mean OH concentration of  $0.99 \times 10^6$  molec/cm<sup>3</sup> (Evans et al. 2005). The  
163 potential long-term variation of global tropospheric OH is evaluated in section 4.

164 The global anthropogenic emission inventory is from EDGAR 3.2FT2000 (Olivier et al.,  
165 2001), but are replaced by the following regional emission inventories: the US Environmental  
166 Protection Agency National Emission Inventory (NEI) for 2008 in North America, the Criteria Air

167 Contaminants (CAC) inventory for Canada, the Big Bend Regional Aerosol and Visibility  
168 Observational (BRAVO) Study Emissions Inventory for Mexico (Kuhns et al. 2003), the  
169 Cooperative Program for Monitoring and Evaluation of the Long-range Transmission of Air  
170 Pollutants in Europe (EMEP) inventory for Europe in 2000 (Vestreng et al. 2002) and the INTEX-  
171 B Asia emissions inventory for 2006 (Zhang et al. 2009). Biomass burning emissions are based on  
172 the Global Fire Emission Database (GFED3, van der Werf et al. 2010). The a priori biomass  
173 burning emissions in Sep-Nov 2006 were applied to Sep-Nov 2015 over Indonesia. Additional CO  
174 sources come from oxidation of methane and biogenic volatile organic compounds (VOCs) as  
175 described in previous studies (Kopacz et al. 2010; Jiang et al. 2013). The biogenic emissions are  
176 simulated using the Model of Emissions of Gases and Aerosols from Nature, version 2.0  
177 (MEGANv2.0, Guenther et al. 2006). The distribution of the annual mean CO emissions for 2001-  
178 2015 is shown in Figure 2. The annual global sources are 892 Tg CO from fossil fuel, biofuel and  
179 biomass burning, 623 Tg CO from the oxidation of biogenic VOCs, and 876 Tg CO from the  
180 oxidation of CH<sub>4</sub>.

181 **3. Inversion Approach**

182 We use the 4D-var data assimilation system in GEOS-Chem (Henze et al. 2007) to  
183 constrain the CO sources. In this approach, we minimize the cost function defined as:

184 
$$J(x) = \sum_{i=1}^N [F_i(x) - z_i]^T S_{\Sigma}^{-1} [F_i(x) - z_i] + (x - x_a)^T S_a^{-1} (x - x_a) \quad (2)$$

185 where  $x$  is the state vector of CO emissions,  $N$  is the number of MOPITT observations that are  
186 distributed in time over the assimilation period,  $z_i$  is a given MOPITT measurement, and  $F(x)$  is  
187 the forward model. The temporal resolution of forward model output ( $F(x)$ ) is one hour, and  
188 consequently, the high resolution MOPITT measurements are averaged temporally (one-hour  
189 resolution) and spatially ( $4^{\circ} \times 5^{\circ}$  resolution) to produce grid mean observations. The number ( $N$ ) of

190 grid mean observations in our assimilation window (one month) is around 10000.

191 The error estimates are assumed to be Gaussian, and are given by  $S_{\Sigma}$ , the observational  
192 error covariance matrix, and  $S_a$ , the a priori error covariance matrix, respectively. The Gaussian  
193 assumption excludes important systematic errors, such as biases in OH distribution, long-range  
194 transport and satellite retrievals in the cost function. Due to lack of meaningful information about  
195 the systematic errors, we assume a uniform observation error of 20% without spatial correlation  
196 following our previous studies (Jiang et al. 2011, 2013, 2015a, 2015b). As shown in Figure S1 (see  
197 supplement), we expect limited influences from the assumption of uniform observation error. The  
198 combustion CO sources (fossil fuel, biofuel and biomass burning) and the oxidation source from  
199 biogenic VOCs are combined together, assuming a 50% uniform a priori error. We optimize the  
200 source of CO from the oxidation of CH<sub>4</sub> separately as an aggregated global source, assuming an a  
201 priori uncertainty of 25%.

202 The a posteriori error covariance matrix is the inverse of the Hessian matrix, which is not  
203 stored in the 4D-var optimization scheme. Bousserez et al. (2015) presented an approach to  
204 construct the a posteriori error covariance matrix using the approximation of the Hessian matrix.  
205 As opposed to earlier studies using surface measurements, the high spatial density of  
206 measurements from satellite instruments can effectively suppress the contribution from random  
207 errors in the cost function, leaving systematic errors as the critical factor in the uncertainty. As  
208 shown by Heald et al. (2004), different assumptions about the inversion configuration (systematic  
209 errors) can produce differences in the source estimates that are significantly larger than the a  
210 posteriori errors calculated based on random errors. Consequently, estimates of a posteriori  
211 uncertainties are not provided in this work (e.g. Table 1 and Table 2).

212 Removing the bias in initial conditions is essential for inverse analysis (Jiang et al. 2013),

213 and can be performed with various data assimilation techniques. Model simulations driven by  
214 optimized emissions can provide good initial conditions (e.g. Gonzi et al. 2011; Bruhwiler et al.  
215 2014; Deng et al. 2014; Houweling et al. 2014). Alternatively, tracer concentrations can be  
216 modified directly to avoid the effect from long-range transport error (e.g. Kopacz et al. 2009; Jiang  
217 et al. 2013, 2015a). There are also efforts to optimize emissions and concentrations simultaneously  
218 (e.g. Fortems-Cheiney et al. 2011, 2012; Bergamaschi et al. 2013; Yin et al. 2015), however, the  
219 contributions from emissions and concentrations to model bias may be hard to be distinguished.  
220 Figure 3 shows the methodology of our assimilation system. Following our previous studies (Jiang  
221 et al. 2013, 2015a, 2015b), we produce initial conditions at the beginning of each monthly  
222 assimilation window by assimilating MOPITT data using a sequential Kalman filter. For the results  
223 presented here, the Kalman filter assimilation was carried out from March 1, 2000 to December  
224 31, 2015.

225 Systematic model errors have a critical influence on inverse analysis. Jiang et al. (2013)  
226 found that the modeled CO concentrations from a 10-day forecast simulation have large  
227 discrepancy with assimilated CO fields, because of bias in model convective transport. Jiang et al.  
228 (2015a) demonstrated that free tropospheric CO is more susceptible to the influence of OH bias  
229 than lower tropospheric CO due to the process of long-range transport. Previous studies suggest  
230 the influences of systematic errors can be mitigated by enhancing the contributions from local  
231 emissions to the discrepancy between model and data, while keeping the influence from long-  
232 range transport as low as possible due to sources of uncertainties that are difficult to quantify. For  
233 example, Pifster et al. (2005) constrained biomass burning CO emissions from boreal North  
234 America with optimized CO fields outside the impacted region; Jiang et al. (2015b) indicated that  
235 their regional inversions were more reliable when the boundary conditions were optimized.

236 In this work, we designed a two-step inversion to reduce the effects of these systematic  
237 errors. As shown in Figure 3, we define the ocean scene (red grids) as boundary conditions. In the  
238 first step of our inverse analysis, sequential Kalman filter assimilation, we directly modify CO  
239 concentrations without any change to emissions in order to provide an optimized CO fields as  
240 consistent as possible with MOPITT. In the second step, the optimized CO fields are used to  
241 rewrite CO concentrations over the ocean every hour, while 4D-var inversion is employed to  
242 constrain CO emissions, without any change on CO distribution over ocean. Only MOPITT data  
243 over land (white grids) were assimilated to constrain CO emissions in the second step. In our  
244 previous study (Jiang et al. 2015b), we performed a regional inversion over North America  
245 continent driven with optimized boundary conditions from global-scale simulation by assimilating  
246 MOPITT CO measurements. In this work, we convert the global inversion system to a combination  
247 of several regional inversions, and the optimization on the boundary conditions is exactly the same  
248 as the regional inversion (Jiang et al. 2015b). With the fixed/optimized boundary conditions, the  
249 emission and transport errors from one continent (e.g. North America) will not affect the emission  
250 estimation of another continent (e.g. Europe).

## 251 **4. Results and Discussion**

### 252 **4.1. Long-term variation of global tropospheric OH**

253 The distribution of tropospheric OH has significant influence on the inverse analysis of CO  
254 emissions (Jiang et al. 2011). Various approaches have been employed to improve the OH  
255 distribution in previous studies. Jiang et al. (2013) assimilated MOPITT CO retrievals in full  
256 chemistry model simulation to provide updated OH fields. Miyazaki et al. (2015) demonstrated  
257 that assimilation of Tropospheric Emission Spectrometer (TES) O<sub>3</sub>, Ozone Monitoring Instrument  
258 (OMI) NO<sub>2</sub>, and MOPITT CO can provide a better description of tropospheric OH. There are also

259 recent efforts that have assimilated surface in-situ MCF measurements (Fortems-Cheiney et al.  
260 2011, 2012; Yin et al. 2015). However, because of the uncertainties in model chemistry schemes,  
261 potential bias drifts in satellite remotely sensed observation, and sparse distribution of surface in-  
262 situ measurements, OH abundances provided by these approaches may not be ideal for the  
263 estimation of long-term CO variation.

264 Emissions of MCF are regulated by the Montreal Protocol agreement. The loss rate of MCF  
265 has become a good tool to evaluate the variation of tropospheric OH (e.g. Krol et al. 1998;  
266 Bousquet et al. 2005; Prinn et al. 2005; Montzka et al. 2011). Using the same approach as Montzka  
267 et al. (2011), we assess the variation of tropospheric OH in the period of 2001-2015. Figure 4a  
268 shows the locations of WDCGG sites with MCF measurements, and Figure 4b shows the global  
269 mean MCF concentration in the past 15 years. Similar as Montzka et al. (2011), our result shows  
270 an exponential decrease of MCF concentration. The loss rate of MCF, derived from 12-month  
271 apart of monthly means [e.g.,  $\ln(MCF_{Jan2007}/MCF_{Jan2006})$ ] varies by 0.2% in the past 15 years  
272 (Figure 4c). The interannual variation is more likely due to the sparsity and discontinuity of  
273 measurements. It should be noted that the MCF measurements in the period 2008.5-2009.5 are  
274 subject to some small biases owing to instrumental issues, however, we believe its influence on  
275 our analysis (2001-2015) is small.

276 The small variation of loss rate of MCF demonstrates that the long-term variation of global  
277 mean OH distributions is negligible in the past 15 years. Consequently, the decreasing trend of  
278 tropospheric CO in North Hemisphere is driven by decreasing CO sources, rather than sinks. For  
279 this reason, the default monthly OH fields of GEOS-Chem model (Evans et al. 2005), without  
280 interannual variability, are used in this work to constrain the long-term variation of CO emissions.  
281 Previous study (Krol et al. 1998) has indicated small discrepancy between derived OH trends based

282 on MCF measurements due to various methods. Because the abundances of tropospheric OH have  
283 large regional discrepancies (e.g. Jiang et al. 2015a), it is possible that the actual OH is more  
284 variable at regions lacking MCF measurements (e.g. India and southeast Asia). Furthermore, the  
285 magnitude and seasonality of the default monthly OH fields could also have uncertainty.  
286 Consequently, the magnitude of CO emissions in our analysis may still be affected by biases in  
287 OH, although the two-step assimilation system is designed to suppress their influence.

288 **4.2. Long-term variation of global CO emissions**

289 In this work, we performed monthly inversions for the period of 2001-2015, using  
290 MOPITT column, profile and lower tropospheric profile (lowest three retrieval levels) data to  
291 investigate the influences associated with vertical sensitivity of satellite instrument and model  
292 transport error. Figure 5 shows the CO emission trends for 2001-2015 constrained by these  
293 different datasets. Because of the combination of various emission categories (i.e. anthropogenic,  
294 biomass burning and VOC oxidation) in our methodology, we cannot completely separate the a  
295 posteriori emission estimates from different sources. However, the various spatial and temporal  
296 distribution of emissions sources (e.g. anthropogenic vs. biomass burning) provides valuable  
297 information to distinguish the contribution from each category. In order to further isolate the  
298 influences of biomass burning, the months dominated by biomass burning (biomass burning CO >  
299 50% of total CO emission in an individual grid) are excluded in the trend analysis for  
300 anthropogenic and VOC sources (Figure 5).

301 For anthropogenic sources, all three analyses show significant emission reduction from  
302 North America, Europe and China. The emission estimates constrained with MOPITT column and  
303 profile data suggest increasing CO emissions from India and Southeast Asia. Conversely, the  
304 emission estimate constrained with MOPITT lower tropospheric profile data shows a decreasing

305 trend in this region, and this decreasing trend is also obtained by Yin et al. (2015). In addition to  
306 differences in emissions trends expected for the lower tropospheric profile results due to the  
307 negative bias drift in MOPITT lower tropospheric retrievals (Deeter et al., 2014), we also expect  
308 the full MOPITT profile to provide a stronger constraint in this region where errors in model  
309 convection in this region can have a large effect on CO emissions estimates (Jiang et al., 2013).

310 For biomass burning sources, we found a negative trend over boreal North America, boreal  
311 Asia and South America, and a positive trend over Indonesia that is primarily due to the strong  
312 impacts of El Nino in 2006 and 2015 on biomass burning in this region (e.g. Field et al., 2016).  
313 Our results for biogenic VOCs are inconclusive; the emission estimates constrained with MOPITT  
314 column and profile data show moderate positive trends in the tropics, and slight negative trends in  
315 mid-latitude regions, whereas the emission estimate constrained with MOPITT lower tropospheric  
316 profile data shows a negative trend globally.

#### 317 **4.2.1. Regional analysis for anthropogenic emissions**

318 Figure 6a shows the regional variation of anthropogenic emissions from the United States  
319 (US). The emission estimates constrained with MOPITT column and profile data match very well  
320 with the a priori emissions, whereas the emission estimate constrained with MOPITT lower  
321 tropospheric profile data is much higher. All three analyses demonstrate a significant emission  
322 reduction over our study period. As shown in Table 1, the total anthropogenic CO emission  
323 (constrained with MOPITT profile data) from US is 56.8 Tg in 2015, which is 35% lower than that  
324 in 2001 (87.7 Tg). Figure 7a shows the monthly mean CO concentrations from WDCGG stations  
325 in US, which demonstrates a similar decreasing trend as our analysis. The initial increase at 2001-  
326 2002 could be caused by uncertainties in the data. The decreasing trend is consistent with the US  
327 Environmental Protection Agency (EPA) Emissions Trends Data (<https://www.epa.gov/air->

328 emissions-inventories/air-pollutant-emissions-trends-data), and other observation records for  
329 western US (Gratz et al. 2015), southeast US (Hidy et al. 2014) and North Atlantic (Kumar et al.  
330 2013).

331 Figure 6b shows the regional variation of anthropogenic emissions from Europe. All three  
332 analyses show an underestimation of a priori emissions, suggesting the CO emissions in the EMEP  
333 inventory are too low. Our results show that anthropogenic emissions decrease during the period  
334 of 2001-2007, but are almost unchanged in the following years, which is consistent with the  
335 observations from WDCGG stations (Figure 7b). Recent studies (Hilboll et al. 2013; Schneider et  
336 al. 2015) showed that NO<sub>2</sub> over Europe from SCIAMACHY is decreasing in the period of 2002-  
337 2008, and almost unchanged in the period of 2008-2011. Henschel et al. (2015) indicated that the  
338 unchanged NO<sub>2</sub> over Europe could be caused by European emissions that are failing to achieve  
339 the expected reduction standards. Because anthropogenic CO and NO<sub>2</sub> share some of the same  
340 combustion sources, it is possible that the unchanged CO emission in our analysis is also due to a  
341 failure of emission controls.

342 Figure 6c shows the regional variation of anthropogenic emissions from east China. We  
343 found Chinese anthropogenic emissions are increasing in the period of 2001-2004. Accompanied  
344 with the global economy recession, the total anthropogenic CO emission (constrained with  
345 MOPITT profile data) from east China decreases to 175.4 Tg in 2008, which is 15% lower than  
346 that in 2004 (205.6 Tg). Our analysis shows a temporary increase of Chinese emissions in 2009  
347 (185.9 Tg), followed by continuous decrease. The total Chinese anthropogenic CO emission is  
348 159.0 Tg in 2015, which is 7% lower than that in 2001 (170.4 Tg). Using surface in-situ  
349 measurements at Hateruma Island, Tohjima et al. (2014) constrained CO emissions from China  
350 for the period 1999-2010. They found Chinese CO emission increases from 1999-2004, and

351 decreases since 2005. Using a “bottom-up” approach, recent studies (Zhao et al. 2012; Xia et al.  
352 2016) indicated that the growth trend of Chinese CO emissions has been changed since 2005  
353 because of improvements in energy efficiency and emission control regulations (e.g. Liu et al.  
354 2015). Figure 7c shows the observation records from 2 stations in the East China outflow region,  
355 which demonstrate similar variations.

356 Figures 6d-6e show the regional variation of anthropogenic emissions from India and  
357 Southeast Asia. The emission estimates constrained with MOPITT column and profile data  
358 demonstrate significant positive trend in our study period, whereas the emission estimate  
359 constrained with MOPITT lower tropospheric profile data shows a decreasing trend. Schneider et  
360 al. (2015) showed that NO<sub>2</sub> over south Asia from SCIAMACHY is increasing in the period of  
361 2003-2011. Using OMI NO<sub>2</sub> measurements, recent studies (e.g., Duncan et al. 2016) demonstrated  
362 that NO<sub>2</sub> over India has a positive trend during 2005-2015. Observations from Cape Rama (CRI)  
363 station (Figure 7d) demonstrate that CO concentration in 2010-2013 is significantly higher than  
364 that in 2001-2002. For these reasons, we have more confidence in our results that indicate  
365 increasing anthropogenic CO emissions from India and Southeast Asia in the past 15 years. The  
366 trend based on the MOPITT lower-tropospheric data is incorrect because of model error in  
367 convection in this dynamically varying region, and the negative bias drift in MOPITT lower  
368 tropospheric retrievals (Deeter et al., 2014). The total anthropogenic CO emission (constrained  
369 with MOPITT profile data) from India and Southeast Asia is 130.4 Tg in 2015, which is 34%  
370 higher than that in 2001 (97.5 Tg). It should be noted that the inconsistency between our analysis  
371 with Yin et al. (2015) suggests more studies are needed for robust conclusion about the variation  
372 of anthropogenic CO emissions for this region.

373 Although our inverse analysis (constrained with MOPITT profile data) suggests similar

374 anthropogenic CO emissions from East China in 2008 and 2014, Figure 7c demonstrates that mean  
375 CO concentrations over the outflow region of East China are 6 ppb higher in 2014 compared to  
376 2008. Our previous study (Jiang et al. 2015c) indicated that anthropogenic emissions from India  
377 and southeast Asia have an important influence on pollutant concentrations in the east China  
378 outflow region. It is possible that the increase of CO concentration observed by WDCGG stations  
379 in this region is caused by the significant increase of anthropogenic CO emission from India and  
380 southeast Asia. In the most recent 5 years (2011-2015), our results (constrained with MOPITT  
381 profile data) suggested a 20.5 Tg emission reduction from East China, and a 10.1 Tg emission  
382 increase from India and Southeast Asia. Assuming a fixed emission growth rate, projected  
383 anthropogenic CO emissions from India and Southeast Asia will overtake Chinese emissions in  
384 2020, resulting in serious socioeconomic issues on both local and global scales.

385 **4.2.2. Regional analysis for biomass burning emissions**

386 Figure 8 and Table 2 show the regional variation of biomass burning emissions. There are  
387 significant decreasing trends in three regions (i.e. boreal North America, boreal Asia, and South  
388 America). Our results show high biomass burning emissions from boreal North America (mainly  
389 Alaska and western Canada) in 2004 (Figure 8a), which have been reported by previous studies  
390 (e.g. Pfister et al. 2005; Turquety et al. 2007), and also from boreal Asia during 2001-2003 (Figure  
391 8b) due to significant fire activity in Siberia (e.g., Yurganov et al., 2005, Stroppiana et al., 2010).  
392 For South America (Figure 8c), we found higher biomass burning emissions in the periods of 2004-  
393 2007 and 2010, consistent with fire activity reported in previous studies (e.g. Hooghiemstra et al.  
394 2012; Bloom et al. 2015).

395 Figure 8d shows the regional variation of biomass burning emissions from Africa. The fire  
396 activities in Africa demonstrates obvious seasonality: peak in boreal winter for Northern

397 Hemispheric Africa, and in austral winter for Southern Hemispheric Africa. Similar to previous  
398 studies (e.g. Chevallier et al. 2009; Tosca et al. 2015), there is no obvious emission trend in Africa  
399 in the past 15 years. This is also consistent with the burned area trends described by Andela et al.  
400 (2014) which show opposite directions for Northern Africa (decreasing) versus Southern Africa  
401 (increasing) and would have cancelling effects in the trend for the continent as a whole.

402 Our results exhibit two strong biomass burning events in Indonesia, 2006 and 2015,  
403 individually (Figure 8e). Previous studies (e.g. Logan et al. 2008; Zhang et al. 2011; Worden et al.  
404 2013b, 2013c, Field et al., 2016) demonstrate the direct relationship between strong Indonesian  
405 fires and El Niño. Recent studies (Huang et al. 2014; Inness et al. 2015) confirm low biomass  
406 burning activities in Indonesia in the period of 2007-2012. CO emissions from the Indonesian fires  
407 associated with the 2015 El Niño were 92 Tg (for October, 2015, as constrained with MOPITT  
408 profile data), and were about three times higher than the October 2006 El Niño driven fire  
409 emissions (32 Tg). Not including the 2015 El Niño driven fires, our analysis indicates a negative  
410 trend of global biomass burning emissions in the past 15 years, as shown in Figure 11f.

411 **4.3. Changes in tropospheric CO during 2001-2015**

412 In this section, we evaluate our inversion results using independent long-term surface in-  
413 situ measurements from WDCGG stations. Figure 9a shows the annual trend of surface CO  
414 concentration for 2001 – 2015 from WDCGG sites, and from model simulations driven with a  
415 priori emissions. Most WDCGG sites exhibit negative trends in the past 15 years, confirming the  
416 decreasing trend of global tropospheric CO, which is consistent with satellite observations (e.g.  
417 Warner et al. 2013; Worden et al. 2013). There are also stations with positive trends, for example,  
418 Tae-ahn Peninsula (TAP, Korea), Ascension Island (ASC, equatorial Atlantic Ocean), Cape Rama  
419 (CRI, India), Bukit Koto Tabang (BKT, Indonesia) and Cape Grim (CGO, Australia). Globally,

420 the a priori model simulation is in reasonable agreement with WDCGG measurements: both show  
421 negative trends in middle/high latitude, and positive trends in some tropical regions. However,  
422 there are noticeable discrepancies, for example, the surface observation from Yonagunijima  
423 (YON, east China sea) shows a negative trend in our study period, suggesting decreasing trend  
424 from Chinese CO emission, whereas the a priori simulation demonstrates significant positive trend.

425 Figure 9b-9d show the model simulations driven with a posteriori emissions. The a  
426 posteriori emissions constrained with MOPITT lower tropospheric profile data (Figure 9d) results  
427 in unrealistic large CO reduction, which could be caused by the negative bias drift of MOPITT  
428 retrievals at lower troposphere (Deeter et al. 2014) and the influence from possible variability in  
429 model convective transport. The a posteriori emissions constrained with MOPITT column and  
430 profile data have similar comparisons. For example, both of them suggest a negative trend over  
431 east China, consistent with observations from YON, and positive trend over northeast Asia,  
432 consistent with observations from TAP.

433 In order to better compare the discrepancy between model simulation and surface  
434 observations, Figure 9e-9g show the improvement due to a posteriori emissions, derived by  
435  $\text{abs}(\text{Trend}_{\text{aposteriori}} - \text{Trend}_{\text{WDCGG}}) - \text{abs}(\text{Trend}_{\text{apriori}} - \text{Trend}_{\text{WDCGG}})$ . Blue (red) means the a posteriori  
436 emissions improves (degrades) the agreement with WDCGG measurements compared to the  
437 simulated surface CO using a priori emissions, while white indicates no change from the prior. As  
438 shown in Figure 9f, the CO emissions constrained with MOPITT profile data improved the model  
439 simulation for most WDCGG sites in the Northern Hemisphere. The a posteriori emissions  
440 constrained with MOPITT column data are somewhat worse, particularly over Europe, while CO  
441 emissions constrained with MOPITT profile data over Europe give improved comparisons to  
442 WDCGG surface CO measurements. Worden et al. (2010) demonstrated that the degrees of

443 freedom for signal (DFS) of MOPITT multi-spectral profile retrievals (TIR+NIR) is about 1.5-2.0  
444 over land, which is reduced to about 1 DFS when converted to a total column. This reduction in  
445 vertical information in MOPITT column data can affect the the reliability of inverse analysis  
446 results (Jiang et al., 2015a). It should be noticed that the vertical correlation in model simulation  
447 is not considered in our assimilation, which could be another possible reason for this discrepancy.

448 Figure 10a-10d show the long-term mean value of surface CO concentration for 2001 –  
449 2015 from WDCGG sites, and model simulations driven with a priori and a posteriori emissions.  
450 All simulations provide similar results for long-term mean value. Figure 10e-10g show the  
451 improvement due to a posteriori emissions, derived by  $\text{abs}(\text{CO}_{\text{aposteriori}} - \text{CO}_{\text{WDCGG}}) - \text{abs}(\text{CO}_{\text{apriori}} - \text{CO}_{\text{WDCGG}})$ . Figure 10f demonstrates that CO emissions constrained with MOPITT profile data  
452 improved the model simulation in about half of the sites in the Northern Hemisphere, whereas the  
453 a posteriori emissions constrained with MOPITT column data are somewhat worse (Figure 10e).  
454 Evaluating modeled tracer concentrations using surface in-situ measurements is more challenging  
455 than evaluating long-term trends. Important sources of uncertainty include the representation error  
456 (e.g. Chang et al. 2015; Kharol et al. 2015) and vertical mixing of boundary layer (e.g. Castellanos  
457 et al. 2011; Cuchiara et al. 2014).

459 Because our a posteriori simulation, particularly using emissions constrained with  
460 MOPITT profile data, results in significant improvement in the long-term trend, and moderate  
461 improvement in the mean value, we believe these a posteriori estimates provide a better description  
462 for the long-term variation of global CO emissions. A remaining question is to explore how  
463 changes in meterological conditions affect the long-term variation. By fixing CO emissions to  
464 2001 levels, Figure 11a-11b show the long-term trend of modeled surface and column CO during  
465 2001-2015, due only to changes in meterological conditions. At the surface level (Figure 11a), we

466 found changes in meterology result in a moderate positive trend in the Northern Hemisphere,  
467 particularly, over northeast Asia, consistent with observation records from the TAP station; and  
468 significant positive trend in tropics, consistent with observation record from ASC station. On the  
469 other hand, the influence of meterological conditions on column CO (Figure 11b) is much weaker.  
470 The discrepancy between surface and column CO suggests the possible contribution from variable  
471 convective transport. It should be noted that our analysis for the contributions from meterological  
472 conditions could be affected by the discrepancies among various versions of the meterological  
473 fields (i.e. GEOS-4, GEOS-5 and GEOS-FP), and the lack of consistency in model physics of  
474 GEOS-5 (e.g. the transition from GEOS 5.1.0 to GEOS 5.2.0 in late 2008).

475 Figure 11c-11h show the variation of global tropospheric CO due to changes in emissions.  
476 Yin et al. (2015) indicated that the negative trend of tropospheric CO in the Northern Hemisphere  
477 is driven by decreasing anthropogenic emissions from North America, Europe and China. Along  
478 with reductions in anthropogenic emissions (Figure 11c, 11d), we found the decrease of biomass  
479 burning emissions from boreal North America and boreal Asia (Figure 11e, 11f) to be an important  
480 factor for this negative trend. In contrast to the emission reduction from North America, Europe  
481 and China, we found increasing anthropogenic emissions from India and southeast Asia, which  
482 result in a pronounced positive trend of tropospheric CO, while Yin et al. (2015) obtain a negative  
483 trend for this region. This discrepancy requires further study and we will need to test the relative  
484 importance of the primary differences in our methods, i.e., models and inversion approaches,  
485 climatological OH (this study) vs. assimilated surface measurements of CH<sub>4</sub> and MCF to update  
486 OH (Yin et al.) and the use of MOPITT profile vs. column CO retrievals (Yin et al., assimilate  
487 only column CO).

488 **5. Summary**

489 The objective of this work is to investigate the dominant reasons for the observed variation  
490 of global tropospheric CO over the past 15 years. We provide an update for this critical question  
491 and also an updated CO emission estimates for model studies. In particular, we use surface  
492 measurements of MCF to evaluate changes in the sinks of atmospheric CO, and constrain the  
493 sources using MOPITT CO measurements to explain the observed decrease in CO concentrations.  
494 Our two-step approach for estimating global CO emissions mitigates the effects of model errors  
495 from transport and chemistry, as well as measurement bias error.

496 Using the same approach as Montzka et al. (2011), we assess the variation of tropospheric  
497 OH (the primary CO sink) in the period of 2001-2015 using MCF measurements from WDCGG  
498 stations. Our result demonstrates negligible variation of global tropospheric OH in the past 15  
499 years, and consequently we suggest that the global sink of CO due to chemical loss through OH  
500 has not likely changed during this time period. We therefore expect the decreasing trend of  
501 tropospheric CO in North hemisphere (e.g. Warner et al. 2013; Worden et al. 2013; Gratz et al.  
502 2015) to be driven by decreasing CO sources. Total anthropogenic CO emissions from the US  
503 were 56.8 Tg in 2015, which are 35% lower than emissions in 2001 (87.7 Tg). Total anthropogenic  
504 CO emissions from East China were 159.0 Tg in 2015, which are 7% lower than 2001 emissions  
505 (170.4 Tg) and 23% lower than 2004 emissions (205.6 Tg). This pronounced decrease of emissions  
506 from US and China is an indication of progress for fuel efficiency and emission control regulations.  
507 Conversely, our results demonstrate that anthropogenic emissions from Europe decreased from  
508 2001 to 2007 but are almost unchanged during 2008-2015. We also found a significant increase of  
509 anthropogenic emissions for India and Southeast Asia. The total anthropogenic CO emission from  
510 India and southeast Asia is 130.4 Tg in 2015, which is 34% higher than that in 2001 (97.5 Tg).  
511 Assuming the same emission growth rate as 2011-2015, we expect that anthropogenic CO

512 emissions from India and Southeast Asia will be larger than Chinese emissions by 2020.

513 In a recent study, Yin et al. (2015) indicated that the decreasing tropospheric CO in the  
514 Northern Hemisphere is caused by the decrease of anthropogenic emissions from North America,  
515 Europe and China. We find that a decrease of biomass burning emissions from boreal North  
516 America and boreal Asia is also an important contributor for the negative trend. Globally, our  
517 analysis indicates a negative trend of biomass burning emissions in the past 15 years, except in  
518 Indonesia due to the strong biomass burning event in 2015 associated with El Niño. Our results  
519 demonstrate a significant decrease of biomass burning emissions from South America, which  
520 could be associated with the reduction of deforestation in Brazil (Reddington et al. 2015), and the  
521 predominant change from El Niño to La Niña in our study period (Andela et al. 2014). For Africa,  
522 there is no obvious CO emission trend in the past 15 years, consistent with previous results  
523 (Chevallier et al. 2009; Tosca et al. 2015; Andela et al., 2014). Our results are inconclusive in  
524 characterizing the CO sources from oxidation of biogenic VOCs. More efforts are needed in the  
525 future to better understand the mechanism for tropical CO emissions.

526 Our analysis highlights the importance of space-based instruments for monitoring changes  
527 in global pollutant emissions. Our results demonstrate successful emission controls in US and  
528 China over the past 15 years, and suggest that emission controls in Europe may need re-evaluation.  
529 We also recommend more efforts in the future to better understand the regional and global effects  
530 of increasing pollutant emissions from India and Southeast Asia.

531

### 532 **Acknowledgments.**

533 We thank the World Data Centre for Greenhouse Gases (WDCGG) for providing their CO  
534 and MCF data. The National Center for Atmospheric Research (NCAR) is sponsored by the

535 National Science Foundation. The NCAR MOPITT project is supported by the National  
536 Aeronautics and Space Administration (NASA) Earth Observing System (EOS) Program. The  
537 MOPITT team also acknowledges support from the Canadian Space Agency (CSA), the Natural  
538 Sciences and Engineering Research Council (NSERC) and Environment Canada, along with the  
539 contributions of COMDEV (the prime contractor) and ABB BOMEM. MOPITT data sets used in  
540 this study are publicly available at <http://reverb.echo.nasa.gov> and at  
541 <https://eosweb.larc.nasa.gov/datapool>.

542

## 543 **Data availability**

544 The MOPITT data is available at <ftp://l5eil01.larc.nasa.gov/MOPITT/MOP02J.006>. The MCF and  
545 CO measurements from WDCGG is available at <http://ds.data.jma.go.jp/gmd/wdcgg/>.

546

## 547 **References**

548 Andela, N., and van der Werf, G.: Recent trends in African fires driven by cropland expansion and  
549 El Niño to La Niña transition, *Nature Climate Change* 4, 791–795, doi:10.1038/nclimate2313,  
550 2014.

551 Arellano, A., Kasibhatla, P., Giglio, L., Werf, G., Randerson, J. and Collatz, G.: Time-dependent  
552 inversion estimates of global biomass-burning CO emissions using Measurement of Pollution in  
553 the Troposphere (MOPITT) measurements, *J Geophys Res Atmospheres* 1984 2012, 111(D9),  
554 doi:10.1029/2005JD006613, 2006.

555 Bergamaschi, P., Frankenberg, C., Meirink, J., Krol, M., Dentener, F., Wagner, T., Platt, U.,  
556 Kaplan, J., Körner, S., Heimann, M., Dlugokencky, E. and Goede, A.: Satellite chartography of  
557 atmospheric methane from SCIAMACHY on board ENVISAT: 2. Evaluation based on inverse

558 model simulations, J Geophys Res Atmospheres 1984 2012, 112(D2),  
559 doi:10.1029/2006JD007268, 2007.

560 Bergamaschi, P., Frankenberg, C., Meirink, J., Krol, M., Villani, M., Houweling, S., Dentener, F.,  
561 Dlugokencky, E., Miller, J., Gatti, L., Engel, A. and Levin, I.: Inverse modeling of global and  
562 regional CH<sub>4</sub> emissions using SCIAMACHY satellite retrievals, J Geophys Res Atmospheres  
563 1984 2012, 114(D22), doi:10.1029/2009JD012287, 2009.

564 Bergamaschi, P., Houweling, S., Segers, A., Krol, M., Frankenberg, C., Scheepmaker, R.,  
565 Dlugokencky, E., Wofsy, S., Kort, E., Sweeney, C., Schuck, T., Brenninkmeijer, C., Chen, H.,  
566 Beck, V. and Gerbig, C.: Atmospheric CH<sub>4</sub> in the first decade of the 21st century: Inverse  
567 modeling analysis using SCIAMACHY satellite retrievals and NOAA surface measurements, J  
568 Geophys Res Atmospheres, 118(13), 7350–7369, doi:10.1002/jgrd.50480, 2013.

569 Bloom, A., Worden, J., Jiang, Z., Worden, H., Kurosu, T., Frankenberg, C. and Schimel, D.:  
570 Remote-sensing constraints on South America fire traits by Bayesian fusion of atmospheric and  
571 surface data, Geophys Res Lett, 42(4), 1268–1274, doi:10.1002/2014GL062584, 2015.

572 Bousquet, P., Hauglustaine, D. A., Peylin, P., Carouge, C., and Ciais, P.: Two decades of OH  
573 variability as inferred by an inversion of atmospheric transport and chemistry of methyl  
574 chloroform, Atmos. Chem. Phys., 5, 2635-2656, doi:10.5194/acp-5-2635-2005, 2005.

575 Bousserez, N., Henze, D., Perkins, A., Bowman, K., Lee, M., Liu, J., Deng, F. and Jones, D.:  
576 Improved analysis-error covariance matrix for high-dimensional variational inversions:  
577 application to source estimation using a 3D atmospheric transport model, Q J Roy Meteor Soc,  
578 141(690), 1906–1921, doi:10.1002/qj.2495, 2015.

579 Bruhwiler, L., Dlugokencky, E., Masarie, K., Ishizawa, M., Andrews, A., Miller, J., Sweeney, C.,  
580 Tans, P., and Worthy, D.: CarbonTracker-CH<sub>4</sub>: an assimilation system for estimating emissions

581 of atmospheric methane, *Atmos. Chem. Phys.*, 14, 8269-8293, doi:10.5194/acp-14-8269-2014,  
582 2014.

583 Castellanos, P., Marufu, L., Doddridge, B., Taubman, B., Schwab, J., Hains, J., Ehrman, S. and  
584 Dickerson, R.: Ozone, oxides of nitrogen, and carbon monoxide during pollution events over the  
585 eastern United States: An evaluation of emissions and vertical mixing, *J Geophys Res  
586 Atmospheres* 1984 2012, 116(D16), doi:10.1029/2010JD014540, 2011.

587 Chang, K.-L., Guillas, S., and Fioletov, V. E.: Spatial mapping of ground-based observations of  
588 total ozone, *Atmos. Meas. Tech.*, 8, 4487-4505, doi:10.5194/amt-8-4487-2015, 2015.

589 Chevallier, F., Fortems, A., Bousquet, P., Pison, I., Szopa, S., Devaux, M. and Hauglustaine, D.:  
590 African CO emissions between years 2000 and 2006 as estimated from MOPITT observations,  
591 *Biogeosciences*, 6(1), 103–111, doi:10.5194/bg-6-103-2009, 2009.

592 Cuchiara, G. C., Li, X., Carvalho, J. and Rappenglück, B.: Intercomparison of planetary boundary  
593 layer parameterization and its impacts on surface ozone concentration in the WRF/Chem model  
594 for a case study in Houston/Texas, *Atmos. Environ.*, 96, 175–185,  
595 doi:10.1016/j.atmosenv.2014.07.013, 2014.

596 Deeter, M., Worden, H., Gille, J., Edwards, D., Mao, D. and Drummond, J.: MOPITT multispectral  
597 CO retrievals: Origins and effects of geophysical radiance errors, *J Geophys Res Atmospheres*  
598 1984 2012, 116(D15), doi:10.1029/2011JD015703, 2011.

599 Deeter, M. N., Martínez-Alonso, S., Edwards, D. P., Emmons, L. K., Gille, J. C., Worden, H. M.,  
600 Sweeney, C., Pittman, J. V., Daube, B. C., and Wofsy, S. C.: The MOPITT Version 6 product:  
601 algorithm enhancements and validation, *Atmos. Meas. Tech.*, 7, 3623-3632, doi:10.5194/amt-7-  
602 3623-2014, 2014.

603 Deng, F., Jones, D. B. A., Henze, D. K., Bouscerez, N., Bowman, K. W., Fisher, J. B., Nassar, R.,

604 O'Dell, C., Wunch, D., Wennberg, P. O., Kort, E. A., Wofsy, S. C., Blumenstock, T., Deutscher,  
605 N. M., Griffith, D. W. T., Hase, F., Heikkinen, P., Sherlock, V., Strong, K., Sussmann, R., and  
606 Warneke, T.: Inferring regional sources and sinks of atmospheric CO<sub>2</sub> from GOSAT XCO<sub>2</sub> data,  
607 *Atmos. Chem. Phys.*, 14, 3703-3727, doi:10.5194/acp-14-3703-2014, 2014.

608 Duncan, B., Lamsal, L., Thompson, A., Yoshida, Y., Lu, Z., Streets, D., Hurwitz, M. and  
609 Pickering, K.: A space-based, high-resolution view of notable changes in urban NO<sub>x</sub> pollution  
610 around the world (2005–2014), *J Geophys Res Atmospheres*, 121(2), 976–996,  
611 doi:10.1002/2015JD024121, 2016.

612 Evans, M. J., and Jacob, D. J.: Impact of new laboratory studies of N<sub>2</sub>O<sub>5</sub> hydrolysis on global  
613 model budgets of tropospheric nitrogen oxides, ozone, and OH, *Geophys. Res. Lett.*, 32, L09813,  
614 doi:10.1029/2005GL022469, 2005.

615 Field, R. et al., 2015 Indonesian fire activity and smoke pollution show persistent non-linear  
616 sensitivity to El Niño-induced drought, *PNAS*, 2016, 9204–9209, doi: 10.1073/pnas.1524888113

617 Fortems-Cheiney, A., Chevallier, F., Pison, I., Bousquet, P., Szopa, S., Deeter, M. and Clerbaux,  
618 C.: Ten years of CO emissions as seen from Measurements of Pollution in the Troposphere  
619 (MOPITT), *J Geophys Res Atmospheres* 1984 2012, 116(D5), doi:10.1029/2010JD014416,  
620 2011.

621 Fortems-Cheiney, A., Chevallier, F., Pison, I., Bousquet, P., Saunois, M., Szopa, S., Cressot, C.,  
622 Kurosu, T. P., Chance, K., and Fried, A.: The formaldehyde budget as seen by a global-scale  
623 multi-constraint and multi-species inversion system, *Atmos. Chem. Phys.*, 12, 6699-6721,  
624 doi:10.5194/acp-12-6699-2012, 2012.

625 Gonzi, S., Feng, L. and Palmer, P.: Seasonal cycle of emissions of CO inferred from MOPITT  
626 profiles of CO: Sensitivity to pyroconvection and profile retrieval assumptions, *Geophys Res*

627 Lett, 38(8), n/a–n/a, doi:10.1029/2011GL046789, 2011.

628 Gratz, L. E., Jaffe, D. A. and Hee, J. R.: Causes of increasing ozone and decreasing carbon  
629 monoxide in springtime at the Mt. Bachelor Observatory from 2004 to 2013, *Atmos Environ*,  
630 109, 323–330, doi:10.1016/j.atmosenv.2014.05.076, 2015.

631 Guenther, A., Karl, T., Harley, P., Wiedinmyer, C., Palmer, P.I., and Geron, C.: Estimates of global  
632 terrestrial isoprene emissions using MEGAN (Model of Emissions of Gases and Aerosols from  
633 Nature), *Atmos. Chem. Phys.*, 6, 3181-3210, doi:10.5194/acp-6-3181-2006, 2006.

634 Heald, C., Jacob, D., Jones, D., Palmer, P., Logan, J., Streets, D., Sachse, G., Gille, J., Hoffman,  
635 R. and Nehrkorn, T.: Comparative inverse analysis of satellite (MOPITT) and aircraft (TRACE-  
636 P) observations to estimate Asian sources of carbon monoxide, *J Geophys Res Atmospheres* 1984  
637 2012, 109, D23306, doi:10.1029/2004JD005185, 2004.

638 Henschel, S., Tertre, A., Atkinson, R., Querol, X., Pandolfi, M., Zeka, A., Haluza, D., Analitis, A.,  
639 Katsouyanni, K., Bouland, C., Pascal, M., Medina, S. and Goodman, P.: Trends of nitrogen  
640 oxides in ambient air in nine European cities between 1999 and 2010, *Atmos Environ*, 117, 234–  
641 241, doi:10.1016/j.atmosenv.2015.07.013, 2015.

642 Henze, D. K., Hakami, A., and Seinfeld, J. H.: Development of the adjoint of GEOS-Chem, *Atmos.*  
643 *Chem. Phys.*, 7, 2413-2433, doi:10.5194/acp-7-2413-2007, 2007.

644 Hidy, G., Blanchard, C., Baumann, K., Edgerton, E., Tanenbaum, S., Shaw, S., Knipping, E.,  
645 Tombach, I., Jansen, J. and Walters, J.: Chemical climatology of the southeastern United States,  
646 1999–2013, *Atmos Chem Phys*, 14(21), 11893–11914, doi:10.5194/acp-14-11893-2014, 2014.

647 Hilboll, A., Richter, A., and Burrows, J. P.: Long-term changes of tropospheric NO<sub>2</sub> over  
648 megacities derived from multiple satellite instruments, *Atmos. Chem. Phys.*, 13, 4145-4169,  
649 doi:10.5194/acp-13-4145-2013, 2013.

650 Hooghiemstra, P., Krol, M., Leeuwen, T., Werf, G., Novelli, P., Deeter, M., Aben, I. and  
651 Röckmann, T.: Interannual variability of carbon monoxide emission estimates over South  
652 America from 2006 to 2010, *J Geophys Res Atmospheres* 1984 2012, 117(D15), n/a–n/a,  
653 doi:10.1029/2012JD017758, 2012.

654 Houweling, S., Krol, M., Bergamaschi, P., Frankenberg, C., Dlugokencky, E. J., Morino, I.,  
655 Notholt, J., Sherlock, V., Wunch, D., Beck, V., Gerbig, C., Chen, H., Kort, E. A., Röckmann,  
656 T., and Aben, I.: A multi-year methane inversion using SCIAMACHY, accounting for  
657 systematic errors using TCCON measurements, *Atmos. Chem. Phys.*, 14, 3991-4012,  
658 doi:10.5194/acp-14-3991-2014, 2014.

659 Huang, L., Fu, R., and Jiang, J. H.: Impacts of fire emissions and transport pathways on the  
660 interannual variation of CO in the tropical upper troposphere, *Atmos. Chem. Phys.*, 14, 4087-  
661 4099, doi:10.5194/acp-14-4087-2014, 2014.

662 Inness, A., Benedetti, A., Flemming, J., Huijnen, V., Kaiser, J. W., Parrington, M., and Remy, S.:  
663 The ENSO signal in atmospheric composition fields: emission-driven versus dynamically  
664 induced changes, *Atmos. Chem. Phys.*, 15, 9083-9097, doi:10.5194/acp-15-9083-2015, 2015.

665 Jiang, Z., Jones, D., Kopacz, M., Liu, J., Henze, D. and Heald, C.: Quantifying the impact of model  
666 errors on top-down estimates of carbon monoxide emissions using satellite observations, *J  
667 Geophys Res Atmospheres* 1984 2012, 116(D15), doi:10.1029/2010JD015282, 2011.

668 Jiang, Z., Jones, D., Worden, H., Deeter, M., Henze, D., Worden, J., Bowman, K., Brenninkmeijer,  
669 C. and Schuck, T.: Impact of model errors in convective transport on CO source estimates  
670 inferred from MOPITT CO retrievals, *J Geophys Res Atmospheres*, 118(4), 2073–2083,  
671 doi:10.1002/jgrd.50216, 2013.

672 Jiang, Z., Jones, D., Worden, H. and Henze, D.: Sensitivity of top-down CO source estimates to

673 the modeled vertical structure in atmospheric CO, *Atmos Chem Phys*, 15(3), 1521–1537,  
674 doi:10.5194/acp-15-1521-2015, 2015a.

675 Jiang, Z., Jones, D., Worden, J., Worden, H., Henze, D. and Wang, Y.: Regional data assimilation  
676 of multi-spectral MOPITT observations of CO over North America, *Atmos Chem Phys*, 15(12),  
677 6801–6814, doi:10.5194/acp-15-6801-2015, 2015b.

678 Jiang, Z., Worden, J. R., Jones, D. B. A., Lin, J.-T., Verstraeten, W. W., and Henze, D. K.:  
679 Constraints on Asian ozone using Aura TES, OMI and Terra MOPITT, *Atmos. Chem. Phys.*, 15,  
680 99–112, doi:10.5194/acp-15-99-2015, 2015c.

681 Jones, D., Bowman, K., Logan, J., Heald, C., Liu, J., Luo, M., Worden, J. and Drummond, J.: The  
682 zonal structure of tropical O<sub>3</sub> and CO as observed by the Tropospheric Emission Spectrometer  
683 in November 2004 – Part 1: Inverse modeling of CO emissions, *Atmos Chem Phys*, 9(11), 3547–  
684 3562, doi:10.5194/acp-9-3547-2009, 2009.

685 Kharol, S. K., Martin, R. V., Philip, S., Boys, B., Lamsal, L. N., Jerrett, M., Brauer, M., Crouse,  
686 D. L., McLinden, C. and Burnett, R. T.: Assessment of the magnitude and recent trends in  
687 satellite-derived ground-level nitrogen dioxide over North America, *Atmos Environ*, 118, 236–  
688 245, doi:10.1016/j.atmosenv.2015.08.011, 2015.

689 Kopacz, M., Jacob, D., Henze, D., Heald, C., Streets, D. and Zhang, Q.: Comparison of adjoint  
690 and analytical Bayesian inversion methods for constraining Asian sources of carbon monoxide  
691 using satellite (MOPITT) measurements of CO columns, *J Geophys Res Atmospheres* 1984  
692 2012, 114(D4), doi:10.1029/2007JD009264, 2009.

693 Kopacz, M., Jacob, D., Fisher, J., Logan, J., Zhang, L., Megretskaya, I., Yantosca, R., Singh, K.,  
694 Henze, D., Burrows, J., Buchwitz, M., Khlystova, I., McMillan, W., Gille, J., Edwards, D.,  
695 Eldering, A., Thouret, V. and Nedelec, P.: Global estimates of CO sources with high resolution

696 by adjoint inversion of multiple satellite datasets (MOPITT, AIRS, SCIAMACHY, TES), Atmos  
697 Chem Phys, 10(3), 855–876, doi:10.5194/acp-10-855-2010, 2010.

698 Krol, M., vanLeeuwen, P. J., and Lelieveld, J.: Global OH trend inferred from methylchloroform  
699 measurements, J. Geophys. Res., 103(D9), 10697–10711, doi:[10.1029/98JD00459](https://doi.org/10.1029/98JD00459), 1998.

700 Kuhns, H., Green, M. and Etyemezian, V.: Big Bend Regional Aerosol and Visibility  
701 Observational (BRAVO) Study Emissions Inventory, Report prepared for BRAVO Steering  
702 Committee, Desert Research Institute, Las Vegas, Nevada, 2003.

703 Kumar, A., Wu, S., Weise, M. F., Honrath, R., Owen, R. C., Helmig, D., Kramer, L., Val Martin,  
704 M., and Li, Q.: Free-troposphere ozone and carbon monoxide over the North Atlantic for 2001–  
705 2011, Atmos. Chem. Phys., 13, 12537–12547, doi:10.5194/acp-13-12537-2013, 2013.

706 Lelieveld, J., Dentener, F., Peters, W. and Krol, M.: On the role of hydroxyl radicals in the self-  
707 cleansing capacity of the troposphere, Atmos Chem Phys, 4(9/10), 2337–2344, doi:10.5194/acp-  
708 4-2337-2004, 2004.

709 Liu, F., Zhang, Q., Tong, D., Zheng, B., Li, M., Huo, H., and He, K. B.: High-resolution inventory  
710 of technologies, activities, and emissions of coal-fired power plants in China from 1990 to 2010,  
711 Atmos. Chem. Phys., 15, 13299–13317, doi:10.5194/acp-15-13299-2015, 2015.

712 Logan, J., Megretskaya, I., Nassar, R., Murray, L., Zhang, L., Bowman, K., Worden, H. and Luo,  
713 M.: Effects of the 2006 El Niño on tropospheric composition as revealed by data from the  
714 Tropospheric Emission Spectrometer (TES), Geophys Res Lett, 35(3),  
715 doi:10.1029/2007GL031698, 2008.

716 Meirink, J., Bergamaschi, P., Frankenberg, C., Amelio, M. d', Dlugokencky, E., Gatti, L.,  
717 Houweling, S., Miller, J., Röckmann, T., Villani, M. and Krol, M.: Four-dimensional variational  
718 data assimilation for inverse modeling of atmospheric methane emissions: Analysis of

719 SCIAMACHY observations, *J Geophys Res Atmospheres* 1984–2012, 113(D17),  
720 doi:10.1029/2007JD009740, 2008.

721 Miyazaki, K., Eskes, H. and Sudo, K.: A tropospheric chemistry reanalysis for the years 2005–  
722 2012 based on an assimilation of OMI, MLS, TES, and MOPITT satellite data, *Atmos Chem*  
723 *Phys*, 15(14), 8315–8348, doi:10.5194/acp-15-8315-2015, 2015.

724 Montzka, S. A., Krol, M., Dlugokencky, E., Hall, B., Jöckel, P., Lelieveld, J.: Small Interannual  
725 Variability of Global Atmospheric Hydroxyl, *Science*, 331(6013), 67–69,  
726 10.1126/science.1197640, 2011.

727 Ohara, T., Akimoto, H., Kurokawa, J., Horii, N., Yamaji, K., Yan, X. and Hayasaka, T.: An Asian  
728 emission inventory of anthropogenic emission sources for the period 1980–2020, *Atmos Chem*  
729 *Phys*, 7(16), 4419–4444, doi:10.5194/acp-7-4419-2007, 2007.

730 Pfister, G., Hess, P., Emmons, L., Lamarque, J. -F., Wiedinmyer, C., Edwards, D., Pétron, G.,  
731 Gille, J. and Sachse, G.: Quantifying CO emissions from the 2004 Alaskan wildfires using  
732 MOPITT CO data, *Geophys Res Lett*, 32(11), doi:10.1029/2005GL022995, 2005.

733 Prinn, R., Huang, J., Weiss, R., Cunnold, D., Fraser, P., Simmonds, P., McCulloch, A., Harth, C.,  
734 Reimann, S., Salameh, P., O'Doherty, S., Wang, R., Porter, L., Miller, B. and Krummel, P.:  
735 Evidence for variability of atmospheric hydroxyl radicals over the past quarter century, *Geophys*  
736 *Res Lett*, 32(7), n/a–n/a, doi:10.1029/2004GL022228, 2005.

737 Reddington, C., Butt, E., Ridley, D., Artaxo, P., Morgan, W., Coe, H. and Spracklen, D.: Air  
738 quality and human health improvements from reductions in deforestation-related fire in Brazil,  
739 *Nat Geosci*, 8(10), 768–771, doi:10.1038/ngeo2535, 2015.

740 Schneider, P., Lahoz, W. A., and van der A, R.: Recent satellite-based trends of tropospheric  
741 nitrogen dioxide over large urban agglomerations worldwide, *Atmos. Chem. Phys.*, 15, 1205–

742 1220, doi:10.5194/acp-15-1205-2015, 2015.

743 Spivakovsky, C. M., Logan, J. A., Montzka, S. A., Balkanski, Y. J., Foreman-Fowler, M., Jones,  
744 D. B. A., Horowitz, L. W., Fusco, A. C., Brenninkmeijer, C. A. M., Prather, M. J., Wofsy, S. C.  
745 and McElroy, M. B.: Three-dimensional climatological distribution of tropospheric OH Update  
746 and evaluation, *J. Geophys. Res.*, 105(D7), 8931–8980, doi:10.1029/1999JD901006, 2000.

747 Streets, D., Zhang, Q., Wang, L., He, K., Hao, J., Wu, Y., Tang, Y. and Carmichael, G.: Revisiting  
748 China's CO emissions after the Transport and Chemical Evolution over the Pacific (TRACE-P)  
749 mission: Synthesis of inventories, atmospheric modeling, and observations, *J Geophys Res  
750 Atmospheres* 1984–2012, 111(D14), doi:10.1029/2006JD007118, 2006.

751 Strode, S., Worden, H., Damon, M., Douglass, A., Duncan, B., Emmons, L., Lamarque, J.-F.,  
752 Manyin, M., Oman, L., Rodriguez, J., Strahan, S. and Tilmes, S.: Interpreting space-based trends  
753 in carbon monoxide with multiple models, *Atmos. Chem. Phys.*, 16(11), 7285–7294,  
754 doi:10.5194/acp-16-7285-2016, 2016.

755 Stroppiana, D., Brivio, P. A., Grégoire, J.-M., Lioussse, C., Guillaume, B., Granier, C., Mieville,  
756 A., Chin, M., and Pétron, G.: Comparison of global inventories of CO emissions from biomass  
757 burning derived from remotely sensed data, *Atmos. Chem. Phys.*, 10, 12173–12189,  
758 doi:10.5194/acp-10-12173-2010, 2010.

759 Tohjima, Y., Kubo, M., Minejima, C., Mukai, H., Tanimoto, H., Ganshin, A., Maksyutov, S.,  
760 Katsumata, K., Machida, T., and Kita, K.: Temporal changes in the emissions of CH<sub>4</sub> and CO  
761 from China estimated from CH<sub>4</sub> / CO<sub>2</sub> and CO / CO<sub>2</sub> correlations observed at Hateruma Island,  
762 *Atmos. Chem. Phys.*, 14, 1663–1677, doi:10.5194/acp-14-1663-2014, 2014.

763 Tosca, M., Diner, D., Garay, M. and Kalashnikova, O.: Human-caused fires limit convection in  
764 tropical Africa: First temporal observations and attribution, *Geophys. Res. Lett.*, 42(15), 6492–

765 6501, doi:10.1002/2015GL065063, 2015.

766 Turquety, S., Logan, J., Jacob, D., Hudman, R., Leung, F., Heald, C., Yantosca, R., Wu, S.,  
767 Emmons, L., Edwards, D. and Sachse, G.: Inventory of boreal fire emissions for North America  
768 in 2004: Importance of peat burning and pyroconvective injection, *J Geophys Res Atmospheres*  
769 1984 2012, 112(D12), doi:10.1029/2006JD007281, 2007.

770 Turner, A. J., Jacob, D. J., Wecht, K. J., Maasakkers, J. D., Lundgren, E., Andrews, A. E., Biraud,  
771 S. C., Boesch, H., Bowman, K. W., Deutscher, N. M., Dubey, M. K., Griffith, D. W. T., Hase,  
772 F., Kuze, A., Notholt, J., Ohyama, H., Parker, R., Payne, V. H., Sussmann, R., Sweeney, C.,  
773 Velazco, V. A., Warneke, T., Wennberg, P. O., and Wunch, D.: Estimating global and North  
774 American methane emissions with high spatial resolution using GOSAT satellite data, *Atmos.*  
775 *Chem. Phys.*, 15, 7049-7069, doi:10.5194/acp-15-7049-2015, 2015.

776 van der Werf, G. R., Randerson, J. T., Giglio, L., Collatz, G. J., Kasibhatla, P. S., and Arellano Jr.,  
777 A. F.: Interannual variability in global biomass burning emissions from 1997 to 2004, *Atmos.*  
778 *Chem. Phys.*, 6, 3423-3441, doi:10.5194/acp-6-3423-2006, 2006.

779 van der Werf, G. R., Randerson, J. T., Giglio, L., Collatz, G. J., Mu, M., Kasibhatla, P. S.,  
780 Morton, D. C., DeFries, R. S., Jin, Y., and van Leeuwen, T. T.: Global fire emissions and the  
781 contribution of deforestation, savanna, forest, agricultural, and peat fires (1997–2009), *Atmos.*  
782 *Chem. Phys.*, 10, 11707–11735, doi:10.5194/acp-10-11707-2010, 2010.

783 van Leeuwen, T. T. and van der Werf, G. R.: Spatial and temporal variability in the ratio of trace  
784 gases emitted from biomass burning, *Atmos. Chem. Phys.*, 11, 3611-3629, doi:10.5194/acp-11-  
785 3611-2011, 2011.

786 Vestreng, V. and Klein, H.: Emission data reported to UNECE/EMEP. Quality assurance and trend  
787 analysis and Presentation of WebDab, Norwegian Meteorological Institute, Oslo, Norway, MSC-

788 W Status Report, 2002.

789 Warner, J., Carminati, F., Wei, Z., Lahoz, W., and Attié, J.-L.: Tropospheric carbon monoxide  
790 variability from AIRS under clear and cloudy conditions, *Atmos. Chem. Phys.*, 13, 12469-12479,  
791 doi:10.5194/acp-13-12469-2013, 2013.

792 Worden, H., Deeter, M., Edwards, D., Gille, J., Drummond, J. and Nédélec, P.: Observations of  
793 near-surface carbon monoxide from space using MOPITT multispectral retrievals, *J Geophys  
794 Res Atmospheres* 1984 2012, 115(D18), doi:10.1029/2010JD014242, 2010.

795 Worden, H. M., Deeter, M. N., Frankenberg, C., George, M., Nichitiu, F., Worden, J., Aben, I.,  
796 Bowman, K. W., Clerbaux, C., Coheur, P. F., de Laat, A. T. J., Detweiler, R., Drummond, J. R.,  
797 Edwards, D. P., Gille, J. C., Hurtmans, D., Luo, M., Martínez-Alonso, S., Massie, S., Pfister, G.,  
798 and Warner, J. X.: Decadal record of satellite carbon monoxide observations, *Atmos. Chem.  
799 Phys.*, 13, 837-850, doi:10.5194/acp-13-837-2013, 2013.

800 Worden, J., Wecht, K., Frankenberg, C., Alvarado, M., Bowman, K., Kort, E., Kulawik, S., Lee,  
801 M., Payne, V., and Worden, H.: CH<sub>4</sub> and CO distributions over tropical fires during October  
802 2006 as observed by the Aura TES satellite instrument and modeled by GEOS-Chem, *Atmos.  
803 Chem. Phys.*, 13, 3679-3692, doi:10.5194/acp-13-3679-2013, 2013b.

804 Worden, J., Jiang, Z., Jones, D., Alvarado, M., Bowman, K., Frankenberg, C., Kort, E., Kulawik,  
805 S., Lee, M., Liu, J., Payne, V., Wecht, K. and Worden, H.: El Niño, the 2006 Indonesian peat  
806 fires, and the distribution of atmospheric methane, *Geophys Res Lett.*, 40(18), 4938–4943,  
807 doi:10.1002/grl.50937, 2013c.

808 Xia, Y., Zhao, Y. and Nielsen, C.: Benefits of China's efforts in gaseous pollutant control indicated  
809 by the bottom-up emissions and satellite observations 2000–2014, *Atmos Environ.*, 136, 43–53,  
810 doi:10.1016/j.atmosenv.2016.04.013, 2016.

811 Yin, Y., Chevallier, F., Ciais, P., Broquet, G., Fortems-Cheiney, A., Pison, I. and Saunois, M.:  
812 Decadal trends in global CO emissions as seen by MOPITT, *Atmos Chem Phys*, 15(23), 13433–  
813 13451, doi:10.5194/acp-15-13433-2015, 2015.

814 Yurganov, L. N., Duchatelet, P., Dzhola, A. V., Edwards, D. P., Hase, F., Kramer, I., Mahieu, E.,  
815 Mellqvist, J., Notholt, J., Novelli, P. C., Rockmann, A., Scheel, H. E., Schneider, M., Schulz,  
816 A., Strandberg, A., Sussmann, R., Tanimoto, H., Velazco, V., Drummond, J. R., and Gille, J. C.:  
817 Increased Northern Hemispheric carbon monoxide burden in the troposphere in 2002 and 2003  
818 detected from the ground and from space, *Atmos. Chem. Phys.*, 5, 563-573, doi:10.5194/acp-5-  
819 563-2005, 2005.

820 Zhang, Q., Streets, D., Carmichael, G., He, K., Huo, H., Kannari, A., Klimont, Z., Park, I., Reddy,  
821 S., Fu, J., Chen, D., Duan, L., Lei, Y., Wang, L. and Yao, Z.: Asian emissions in 2006 for the  
822 NASA INTEX-B mission, *Atmos Chem Phys*, 9(14), 5131–5153, doi:10.5194/acp-9-5131-2009,  
823 2009.

824 Zhang, L., Li, Q. B., Jin, J., Liu, H., Livesey, N., Jiang, J. H., Mao, Y., Chen, D., Luo, M., and  
825 Chen, Y.: Impacts of 2006 Indonesian fires and dynamics on tropical upper tropospheric carbon  
826 monoxide and ozone, *Atmos. Chem. Phys.*, 11, 10929-10946, doi:10.5194/acp-11-10929-2011,  
827 2011.

828 Zhao, Y., Nielsen, C., McElroy, M., Zhang, L. and Zhang, J.: CO emissions in China: Uncertainties  
829 and implications of improved energy efficiency and emission control, *Atmos Environ*, 49, 103–  
830 113, doi:10.1016/j.atmosenv.2011.12.015, 2012.

831  
832 **Tables and Figures**

833 **Table 1.** Annual total anthropogenic CO emission in different regions, from 2001 to 2015,  
834 constrained with MOPITT column, profile and lower tropospheric data. The region definition is  
835 shown in Figure 2e.

836  
837 **Table 2.** Annual total biomass burning CO emission in different regions, from 2001 to 2015,  
838 constrained with MOPITT column, profile and lower tropospheric data. The region definition is  
839 shown in Figure 2f.

840  
841 **Figure 1.** Difference between MOPITT CO retrievals and HIPPO aircraft measurements. The  
842 aircraft measurements are smoothed with MOPITT averaging kernels. The black solid line shows  
843 the 4-order polynomial curve fitting, which is used to correct MOPITT data in this work.

844  
845 **Figure 2.** (a-d) Mean a priori CO emissions from combustion sources and the oxidation of biogenic  
846 VOCs and CH<sub>4</sub> from 2001 to 2015. The unit is 10<sup>12</sup> molec/cm<sup>2</sup>/sec. (e-f) Region definitions for (e)  
847 anthropogenic and (f) biomass burning sources.

848  
849 **Figure 3.** Schematic diagram for methodology of the assimilation system. Sequential Kalman  
850 Filter was run from March 1 2000 to December 31 2015 to produce the optimized initial conditions  
851 (monthly) and boundary conditions (hourly). Monthly 4-DVAR inversions were performed with  
852 the optimized initial conditions. Only MOPITT data over land (white grids) were assimilated in  
853 the 4-DVAR inversions, while the CO abundances over ocean (red grids) were defined as  
854 boundaries and rewritten using the optimized hourly CO fields from Kalman Filter. The Kalman  
855 filter run is completely independent of the 4-DVAR inversions. There is no feedback of the 4-  
856 DVAR inversion results to the boundary conditions.

857  
858 **Figure 4.** (a) Locations of WDCGG sites with MCF measurements. (b) Global mean MCF  
859 concentration. (c) Exponential loss rate of MCF, derived from 12-month apart of monthly means  
860 [e.g., ln(MCF<sub>Jan2007</sub>/MCF<sub>Jan2006</sub>)]. The black solid line shows the 12-month mean value.

861  
862 **Figure 5.** CO emission trends for 2001 – 2015, constrained with MOPITT column, profile and  
863 lower tropospheric profile data. The months dominated by biomass burning emissions are excluded  
864 from the trend calculation for anthropogenic and biogenic VOC emissions.

865  
866 **Figure 6.** 12-month mean value of anthropogenic CO emissions (with unit Tg/month) for 2001 –  
867 2015: a priori emission (green) and a posteriori emissions constrained with MOPITT column data  
868 (black), MOPITT profile data (blue) and MOPITT lower tropospheric profile data (red). The green  
869 dash line shows the monthly a priori anthropogenic CO emissions. The region definition is shown  
870 in Figure 2e.

871  
872 **Figure 7.** Monthly mean CO concentrations (green) and 12-month mean value (black) from  
873 WDCGG stations for 2001 – 2015. (a) 15-station average in United States (b) 20-station average  
874 in Europe (c) 2-station (YON and JMA) average in east China outflow (4) Cape Rama (CRI) in  
875 India.

876  
877 **Figure 8.** Monthly biomass burning CO emissions (with unit Tg/month) for 2001 – 2015: a priori  
878 emission (green) and a posteriori emissions constrained with MOPITT column data (black),

879 MOPITT profile data (blue) and MOPITT lower tropospheric profile data (red). The region  
880 definition is shown in Figure 2f.

881  
882 **Figure 9.** Panels (a-d): long-term trend (annual) of surface CO concentration for 2001 – 2015 from  
883 WDCGG sites, and model simulations driven with a priori and a posteriori emissions. Panels (e-  
884 g): effect of a posteriori emissions, derived by  $\text{abs}(\text{Trend}_{\text{a posteriori}} - \text{Trend}_{\text{WDCGG}}) - \text{abs}(\text{Trend}_{\text{a priori}} -$   
885  $\text{Trend}_{\text{WDCGG}})$ ; blue (red) means the a posteriori emissions improves (degrades) the agreement with  
886 WDCGG measurements compared to the a priori emissions, while white indicates no change from  
887 the priori. Only stations with more than 10 year observations (the time range between the first and  
888 last observations) during 2001-2015 are included.

889  
890 **Figure 10.** Panels (a-d): long-term mean value of surface CO concentration for 2001 – 2015 from  
891 WDCGG sites, and model simulations driven with a priori and a posteriori emissions. Panels (e-  
892 g): effect of a posteriori emissions, derived by  $\text{abs}(\text{CO}_{\text{a posteriori}} - \text{CO}_{\text{WDCGG}}) - \text{abs}(\text{CO}_{\text{a priori}} -$   
893  $\text{CO}_{\text{WDCGG}})$ ; blue (red) means the a posteriori emissions improves (degrades) the agreement with  
894 WDCGG measurements compared to the a priori emissions, while white indicates no change from  
895 the priori. Only stations with more than 10 year observations (the time range between the first and  
896 last observations) during 2001-2015 are included.

897  
898 **Figure 11.** Long-term trend (annual) of modeled surface and column CO for 2001 – 2015 with (a-  
899 b) all emission sources are fixed at 2001 level. (c-d) variable anthropogenic emissions; (e-f)  
900 variable biomass burning emissions; (g-h) variable biogenic VOCs emissions; The variable  
901 emissions are constrained with MOPITT profile data.

Years	MOPITT Column (Tg/year)					MOPITT Profile (Tg/year)					MOPITT Lower Profile (Tg/year)				
	United States	Europe	E China	India/SE Asia	Gobal Total	United States	Europe	E China	India/SE Asia	Gobal Total	United States	Europe	E China	India/SE Asia	Gobal Total
2001	87.8	71.6	165.7	102.2	526.5	87.7	77.3	170.4	97.5	522.9	112.9	92.0	215.7	136.1	677.5
2002	84.1	65.9	171.3	93.3	508.9	82.3	77.1	176.1	81.1	504.2	110.1	89.8	221.9	119.8	658.2
2003	80.8	65.3	178.8	95.4	516.2	80.4	74.5	189.2	88.5	523.2	103.6	87.0	218.1	121.9	645.1
2004	77.4	65.5	178.5	105.0	524.5	91.1	83.8	205.6	113.8	596.6	103.0	89.5	222.8	124.6	652.7
2005	72.7	64.6	178.6	104.3	518.0	82.6	79.4	200.6	116.8	581.5	92.7	84.5	215.3	126.2	630.6
2006	74.6	61.5	172.7	98.1	500.7	85.6	74.5	197.7	111.0	567.6	93.9	78.9	205.1	118.1	603.1
2007	73.7	56.5	177.1	105.8	511.4	84.0	67.9	200.9	113.2	568.2	90.9	71.8	208.1	119.4	599.6
2008	67.1	55.5	150.2	102.1	473.5	77.2	65.4	175.4	110.2	530.8	83.9	69.6	175.0	111.1	548.4
2009	66.0	54.8	162.0	105.7	486.0	74.5	65.1	185.9	118.3	544.1	78.0	67.0	184.5	115.1	547.4
2010	59.2	54.5	159.3	100.5	470.6	67.8	65.3	183.1	112.8	529.6	73.5	69.0	185.5	106.7	539.1
2011	53.5	52.9	153.2	107.4	461.9	60.5	63.1	179.5	120.3	522.1	63.0	65.6	175.7	107.5	511.0
2012	54.9	58.3	167.0	113.8	496.2	58.2	65.2	184.2	128.8	540.8	62.5	68.9	187.0	115.7	540.7
2013	54.3	62.6	160.4	120.9	503.0	56.7	68.8	171.2	131.3	532.2	61.8	73.8	176.8	114.6	531.5
2014	55.0	60.1	157.1	121.3	499.4	56.8	63.9	175.6	133.4	533.4	60.9	68.5	174.4	115.5	523.5
2015	55.1	61.4	145.1	115.6	484.7	56.8	66.9	159.0	130.4	520.2	59.5	69.3	160.5	109.2	504.3

902

**Table 1.** Annual total anthropogenic CO emission in different regions, from 2001 to 2015, constrained with MOPITT column, profile and lower tropospheric data. The region definition is shown in Figure 2e.

906

907

908

909

Years	MOPITT Column (Tg/year)						MOPITT Profile (Tg/year)						MOPITT Lower Profile (Tg/year)					
	Boreal North America	Boreal Asia	South America	Africa	SE Asia	Gobal Total	Boreal North America	Boreal Asia	South America	Africa	SE Asia	Gobal Total	Boreal North America	Boreal Asia	South America	Africa	SE Asia	Gobal Total
2001	1.2	24.8	25.5	160.8	14.0	272.4	1.2	26.5	28.4	153.5	9.5	267.7	1.3	28.4	31.9	222.0	21.4	369.6
2002	10.1	23.7	38.4	164.5	44.9	331.5	12.6	50.6	40.7	171.3	36.1	369.2	17.0	65.9	42.1	222.9	67.9	488.3
2003	8.9	47.7	39.6	162.7	17.2	324.2	11.1	65.4	41.4	174.9	14.1	356.2	13.6	76.9	44.0	220.9	24.8	445.2
2004	12.7	4.7	55.3	136.9	39.5	292.3	26.9	5.9	58.4	158.6	44.4	350.1	46.3	6.8	55.7	167.1	46.7	381.1
2005	11.2	7.7	61.8	167.4	29.4	318.4	15.5	9.8	67.3	193.3	31.1	364.9	19.1	11.3	68.1	203.1	34.8	387.3
2006	4.5	11.5	32.9	134.0	51.0	278.0	5.4	14.3	36.3	158.1	68.4	337.6	5.8	15.4	32.9	164.6	77.9	354.9
2007	5.1	10.2	72.9	154.9	19.3	313.4	5.9	12.8	84.6	174.3	23.9	365.8	6.6	13.8	78.4	182.1	23.7	369.3
2008	3.6	19.5	26.9	151.9	10.9	245.9	4.0	25.3	31.1	176.2	13.5	288.4	4.9	26.2	31.3	174.8	13.4	290.4
2009	5.4	11.1	16.4	132.8	36.7	254.8	5.7	12.8	16.9	142.2	37.3	274.1	6.1	13.2	16.8	139.5	38.3	274.2
2010	7.5	13.0	61.8	150.5	15.1	281.9	10.4	16.8	72.4	168.1	20.2	329.1	11.4	19.5	69.1	167.3	20.4	329.6
2011	4.1	13.3	15.1	145.7	11.5	240.3	5.1	15.8	16.6	153.0	15.4	261.5	5.6	16.1	16.3	145.4	13.4	250.8
2012	4.8	15.3	24.9	143.7	13.8	256.1	5.1	16.6	25.5	151.9	16.9	275.6	5.8	17.0	26.5	154.4	16.9	277.1
2013	4.5	11.7	12.4	172.0	13.1	257.6	6.0	12.9	13.9	170.8	22.7	270.1	6.7	13.8	16.0	187.0	14.6	284.4
2014	6.8	13.9	17.9	167.0	21.4	275.4	8.1	15.4	17.3	161.1	25.8	275.6	7.4	15.3	18.6	181.3	19.8	289.6
2015	7.0	14.3	29.3	193.6	66.4	357.7	7.4	15.3	28.0	188.9	162.0	448.1	6.8	14.3	28.1	204.0	87.1	386.5

910

911

912

913

914

915

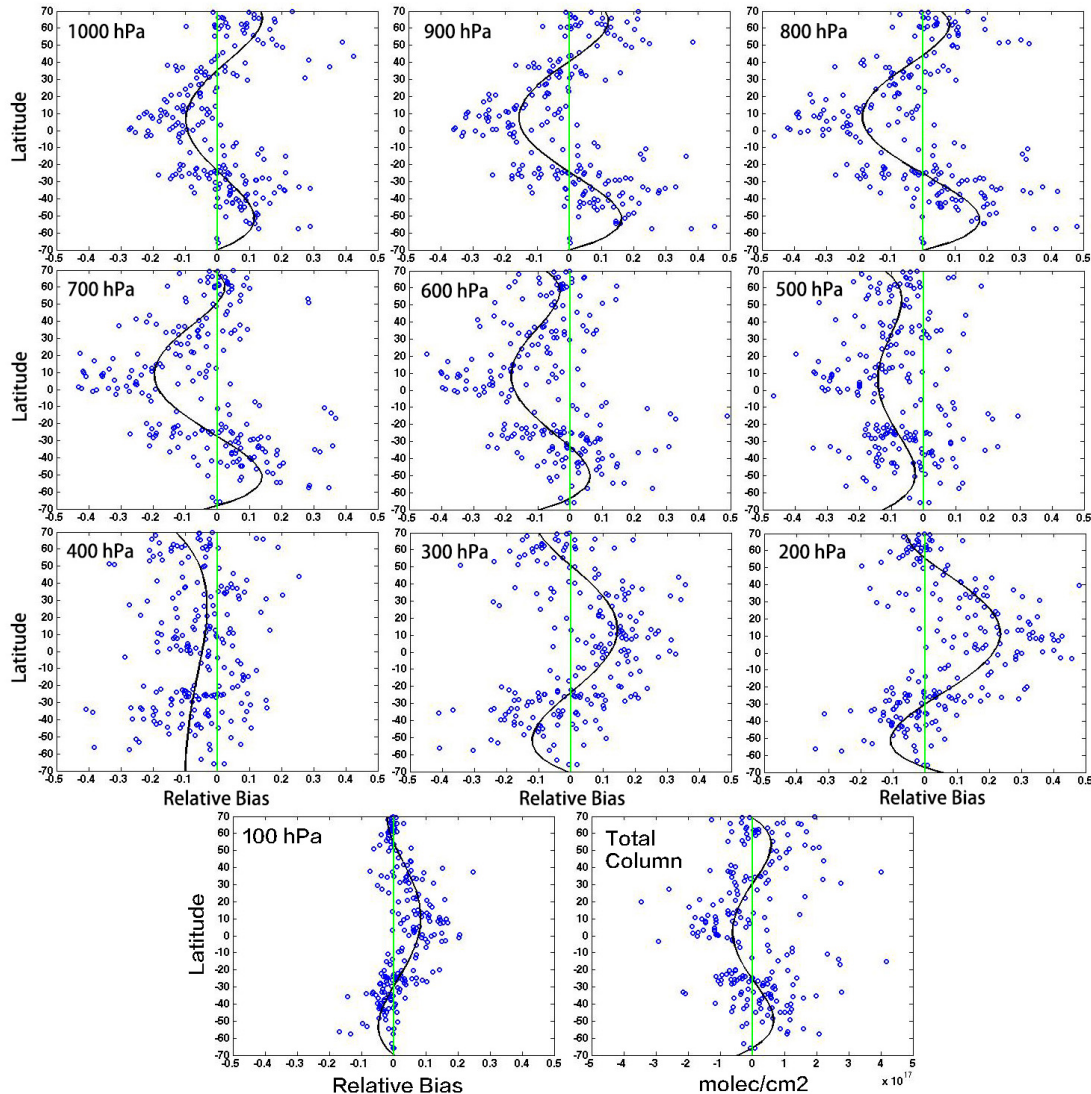
916

917

918

**Table 2.** Annual total biomass burning CO emission in different regions, from 2001 to 2015, constrained with MOPITT column, profile and lower tropospheric data. The region definition is shown in Figure 2f.

919  
920  
921  
922  
923  
924  
925



926

**Figure 1.** Difference between MOPITT CO retrievals and HIPPO aircraft measurements. The aircraft measurements are smoothed with MOPITT averaging kernels. The black solid line shows the 4-order polynomial curve fitting, which is used to correct MOPITT data in this work.

930

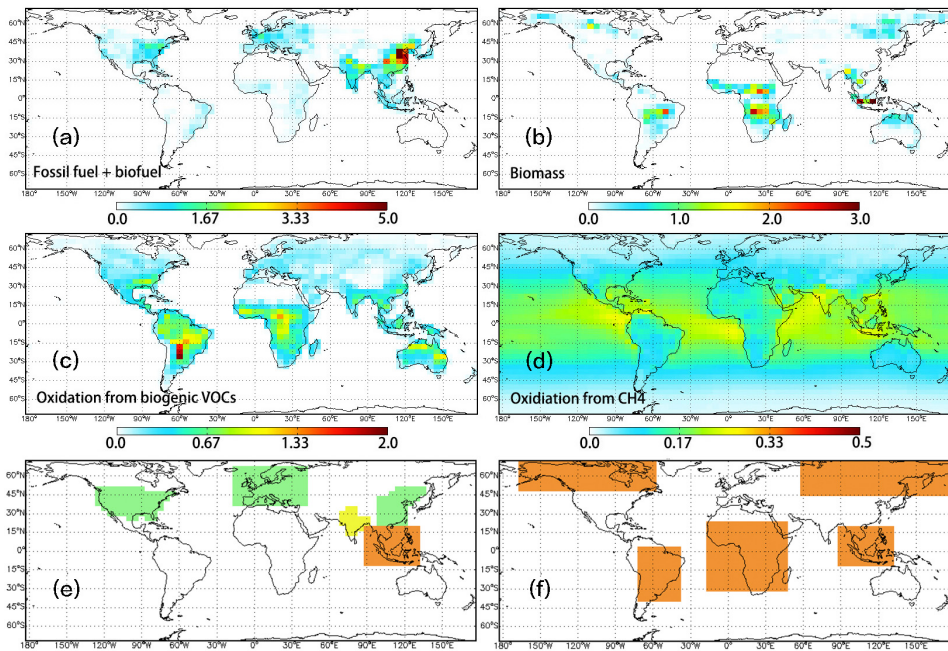
931

932

933

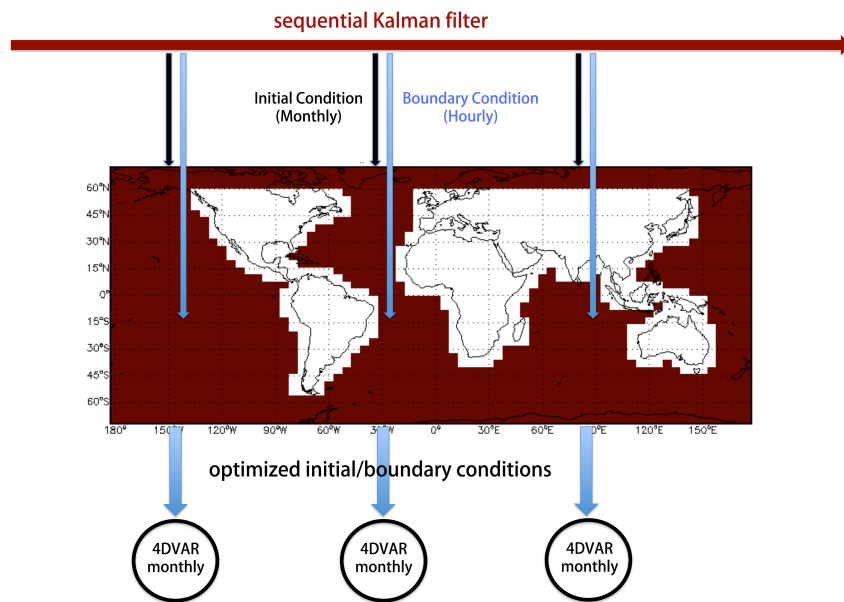
934

935



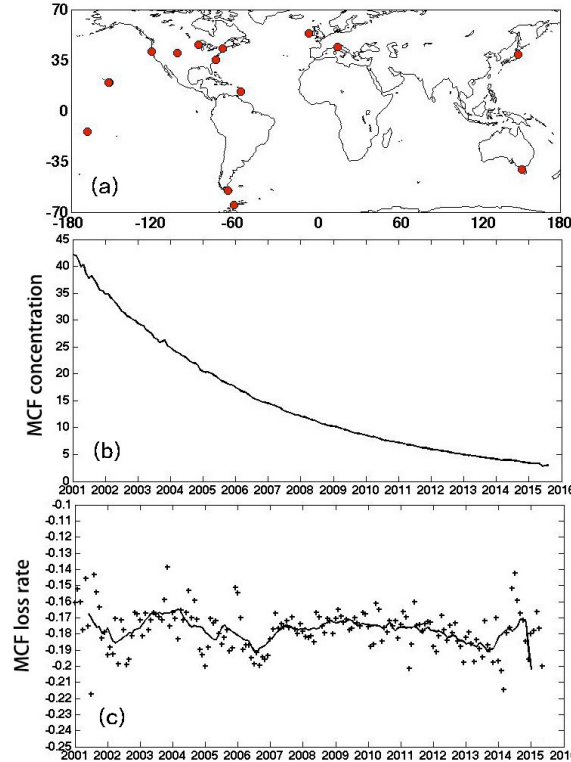
937  
938  
939  
940

**Figure 2.** (a-d) Mean a priori CO emissions from combustion sources and the oxidation of  
939  
940 biogenic VOCs and CH<sub>4</sub> from 2001 to 2015. The unit is 10<sup>12</sup> molec/cm<sup>2</sup>/sec. (e-f) Region  
definitions for (e) anthropogenic and (f) biomass burning sources.



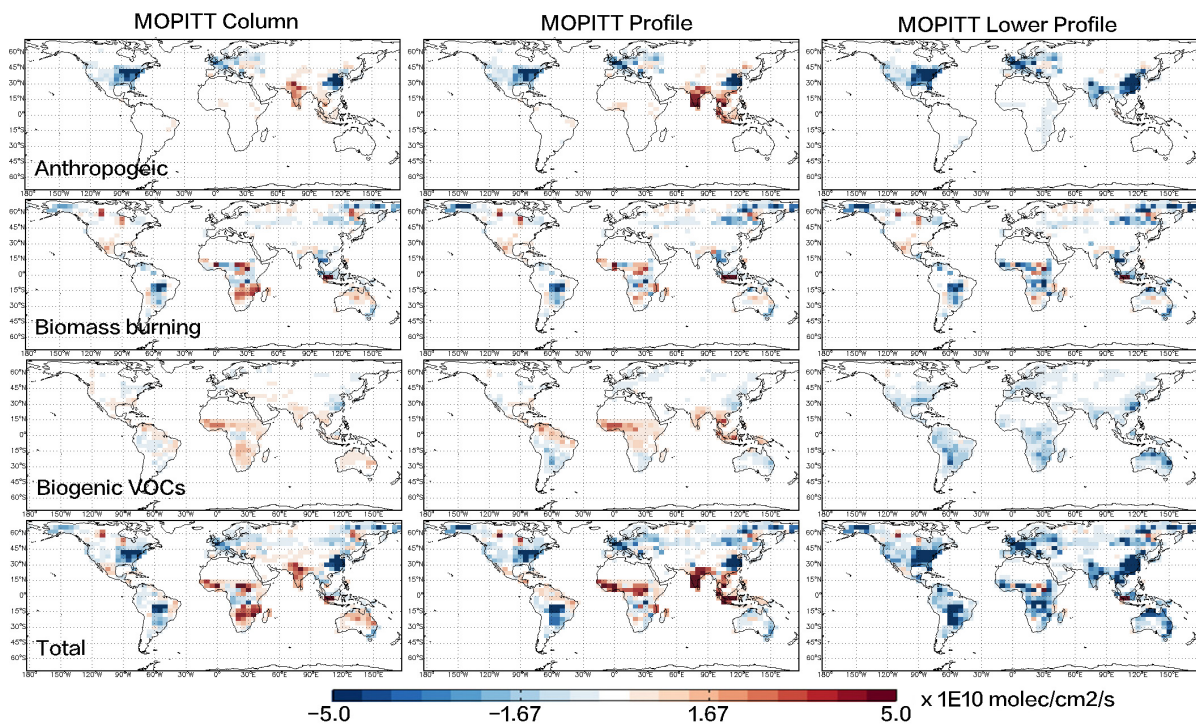
941  
942  
943  
944  
945  
946  
947  
948  
949

**Figure 3.** Schematic diagram for methodology of the assimilation system. Sequential Kalman  
Filter was run from March 1 2000 to December 31 2015 to produce the optimized initial  
conditions (monthly) and boundary conditions (hourly). Monthly 4-DVAr inversions were  
performed with the optimized initial conditions. Only MOPITT data over land (white grids)  
were assimilated in the 4-DVAr inversions, while the CO abundances over ocean (red grids)  
were defined as boundaries and rewritten using the optimized hourly CO fields from Kalman  
Filter. The Kalman filter run is completely independent of the 4-DVAr inversions. There is no  
feedback of the 4-DVAr inversion results to the boundary conditions.



950  
951  
952  
953  
954

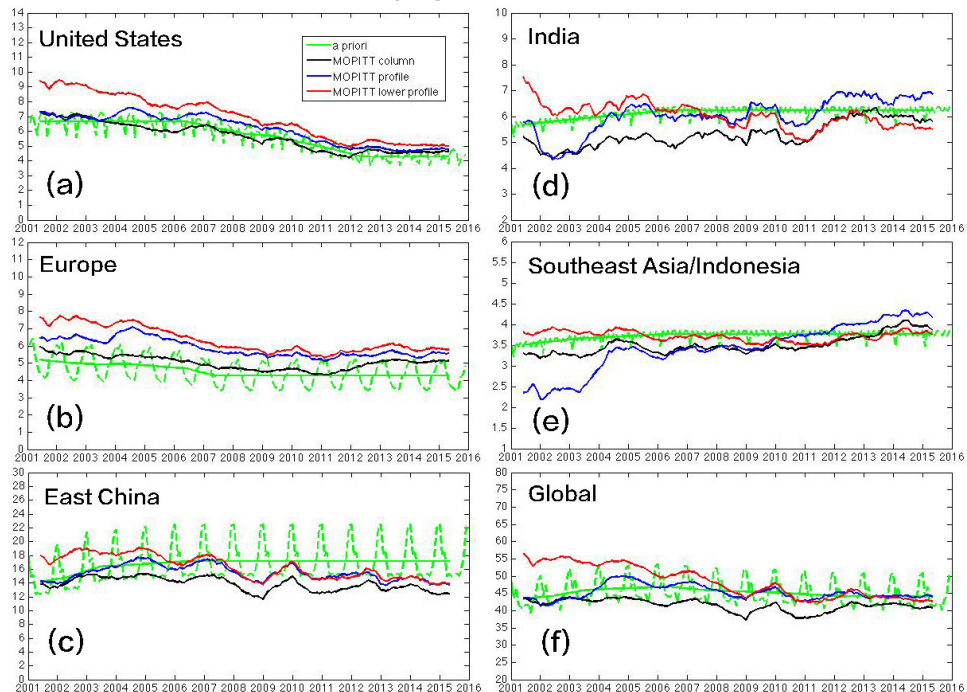
**Figure 4.** (a) Locations of WDCGG sites with MCF measurements. (b) Global mean MCF concentration. (c) Exponential loss rate of MCF, derived from 12-month apart of monthly means [e.g.,  $\ln(MCF_{Jan2007}/MCF_{Jan2006})$ ]. The black solid line shows the 12-month mean value.



955  
956  
957  
958

**Figure 5.** CO emission trends for 2001 – 2015, constrained with MOPITT column, profile and lower tropospheric profile data. The months dominated by biomass burning emissions are excluded from the trend calculation for anthropogenic and biogenic VOC emissions.

### Anthropogenic Emissions

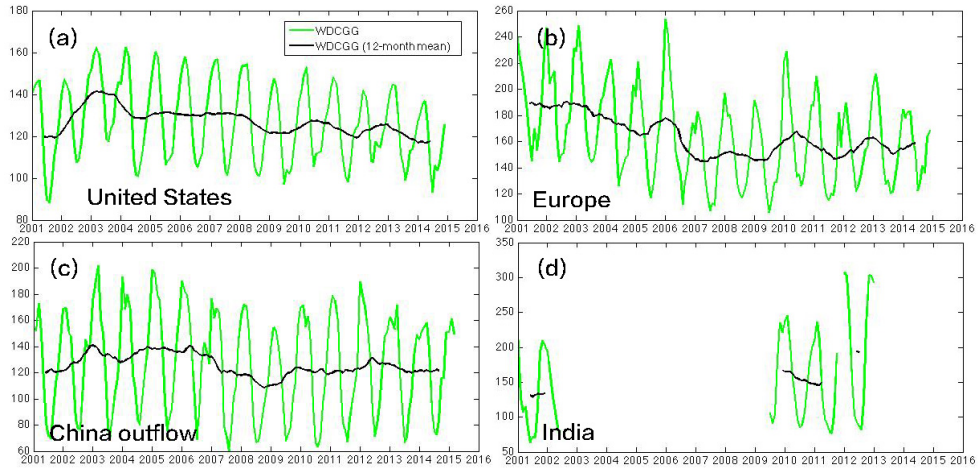


960

961 **Figure 6.** 12-month mean value of anthropogenic CO emissions (with unit Tg/month) for 2001  
962 – 2015: a priori emission (green) and a posteriori emissions constrained with MOPITT column  
963 data (black), MOPITT profile data (blue) and MOPITT lower tropospheric profile data (red).  
964 The green dash line shows the monthly a priori anthropogenic CO emissions. The region  
965 definition is shown in Figure 2e.

966

967



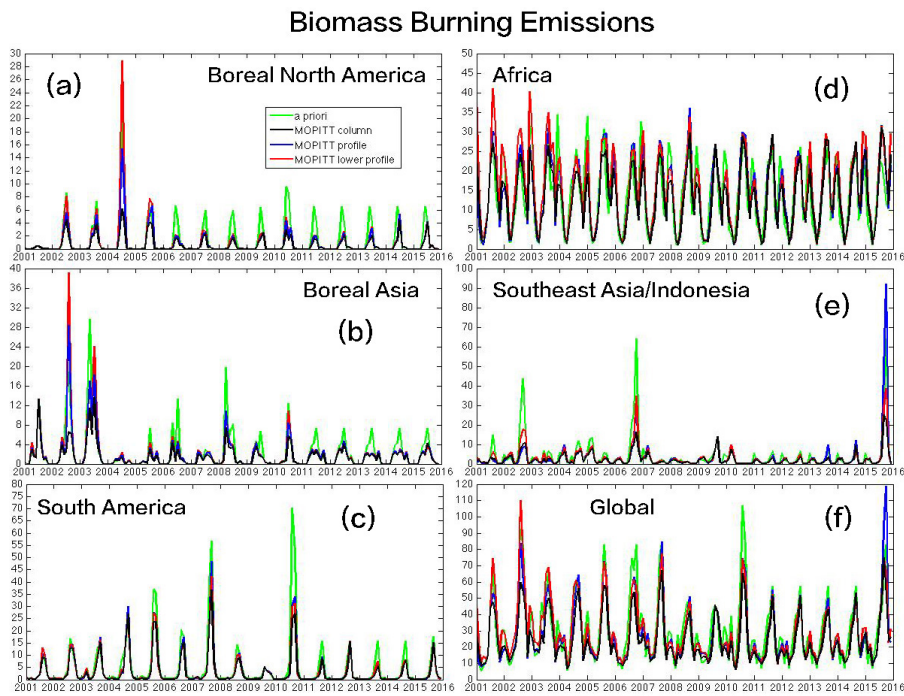
968

969 **Figure 7.** Monthly mean CO concentrations (green) and 12-month mean value (black) from  
970 WDCGG stations for 2001 – 2015. (a) 15-station average in United States (b) 20-station  
971 average in Europe (c) 2-station (YON and JMA) average in east China outflow (4) Cape Rama  
972 (CRI) in India.

973

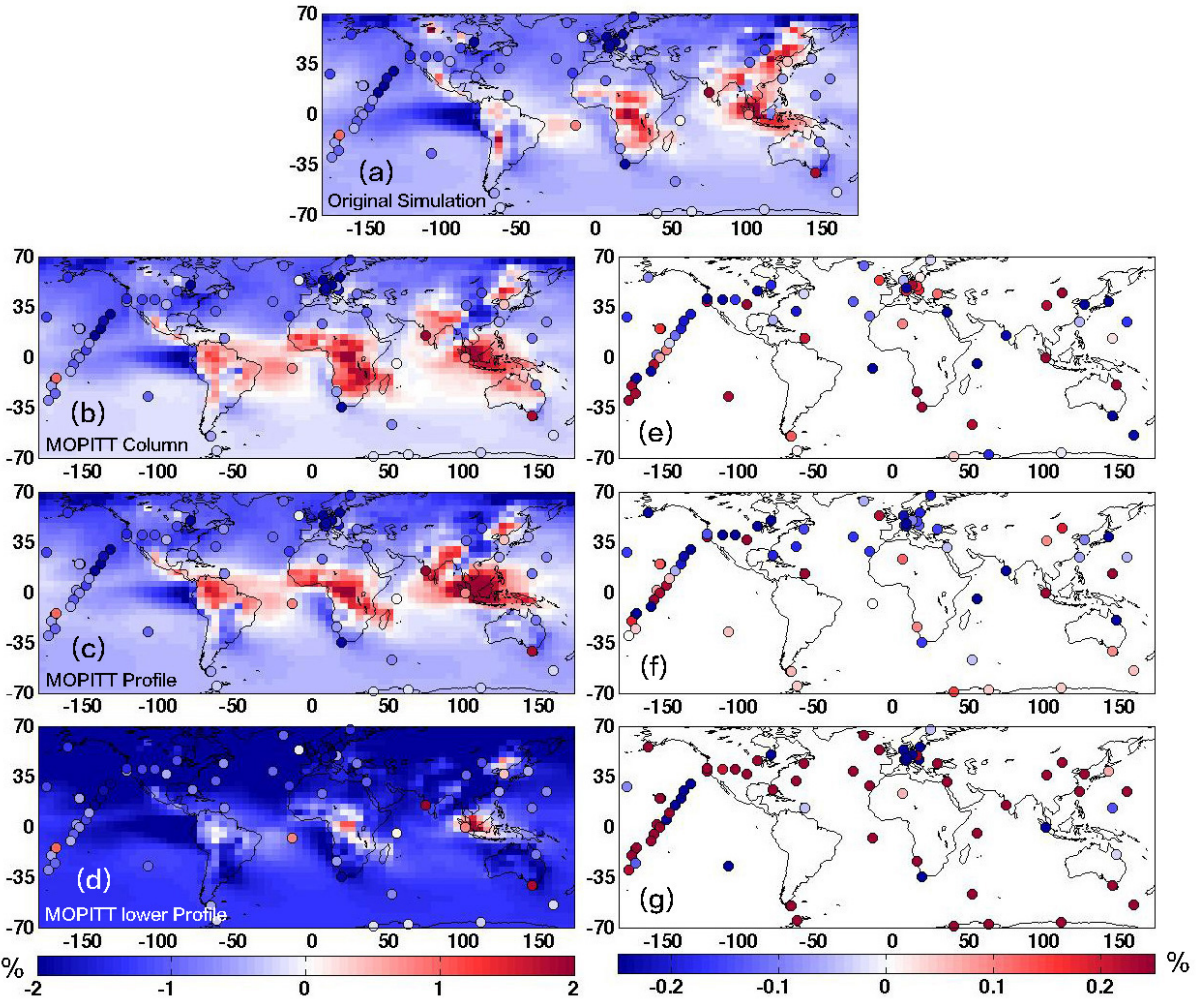
974

975  
976  
977  
978  
979  
980  
981  
982  
983  
984  
985  
986



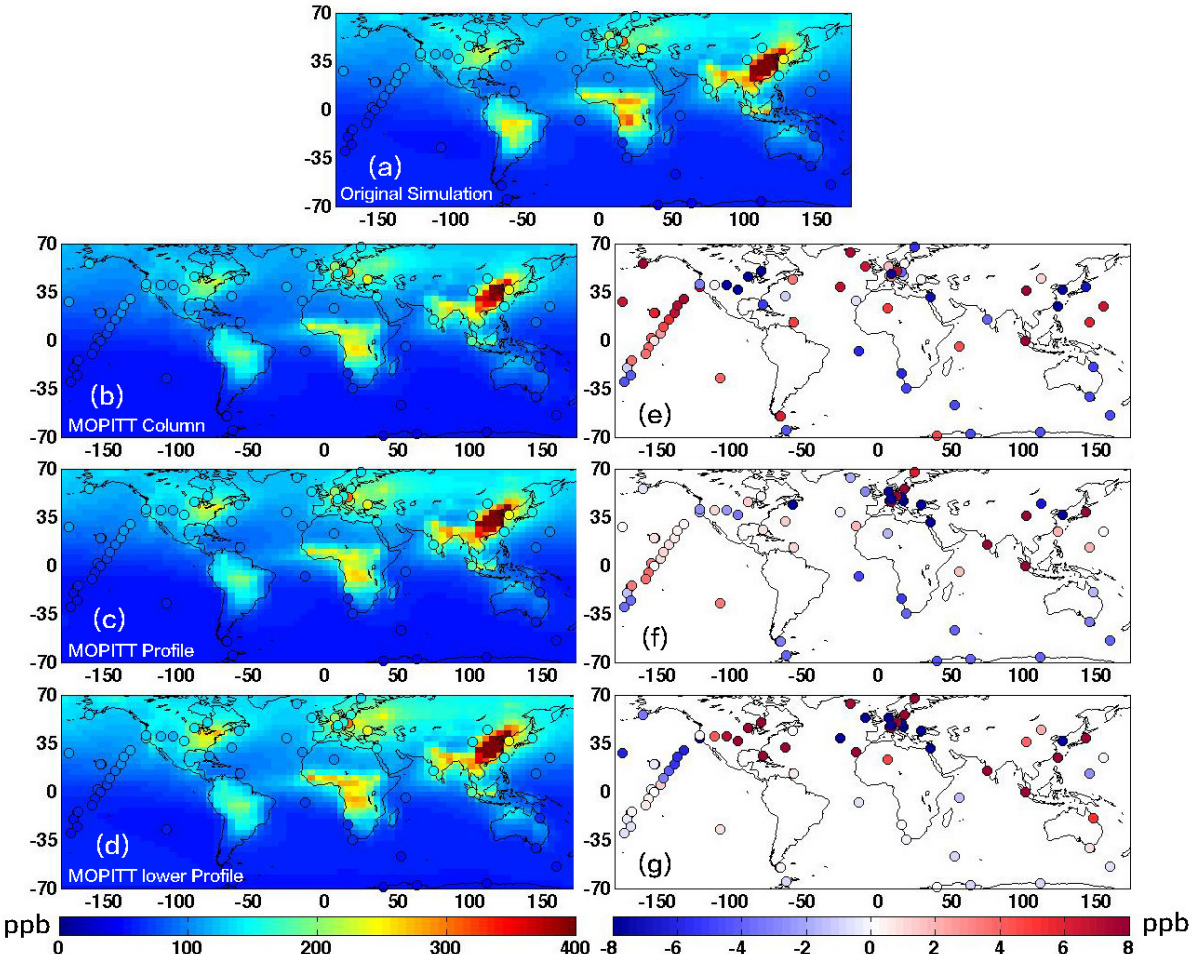
987  
988 **Figure 8.** Monthly biomass burning CO emissions (with unit Tg/month) for 2001 – 2015: a  
989 priori emission (green) and a posteriori emissions constrained with MOPITT column data  
990 (black), MOPITT profile data (blue) and MOPITT lower tropospheric profile data (red). The  
991 region definition is shown in Figure 2f.  
992  
993  
994  
995  
996  
997  
998  
999  
1000  
1001  
1002

1003  
1004  
1005  
1006  
1007



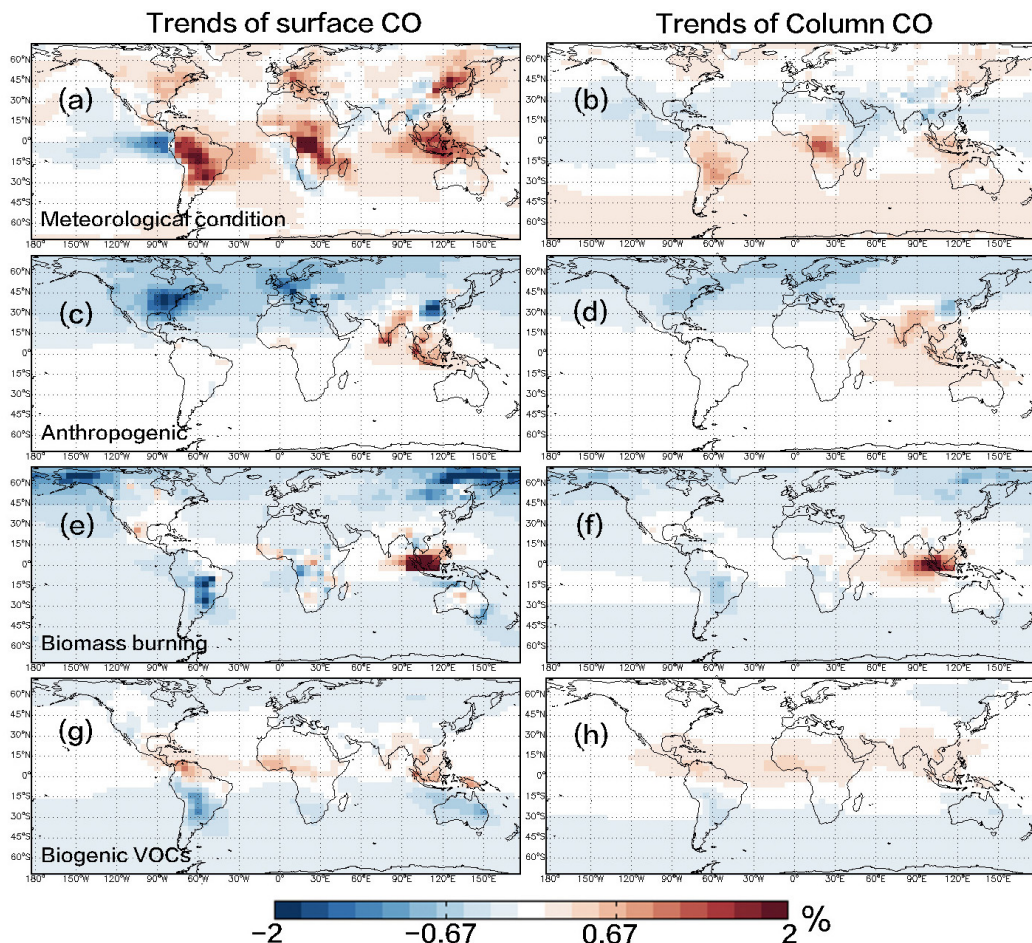
1008  
1009 **Figure 9.** Panels (a-d): long-term trend (annual) of surface CO concentration for 2001 – 2015  
1010 from WDCGG sites, and model simulations driven with a priori and a posteriori emissions.  
1011 Panels (e-g): effect of a posteriori emissions, derived by  $\text{abs}(\text{Trend}_{\text{a posteriori}} - \text{Trend}_{\text{WDCGG}}) -$   
1012  $\text{abs}(\text{Trend}_{\text{a priori}} - \text{Trend}_{\text{WDCGG}})$ ; blue (red) means the a posteriori emissions improves (degrades)  
1013 the agreement with WDCGG measurements compared to the a priori emissions, while white  
1014 indicates no change from the priori. Only stations with more than 10 year observations (the  
1015 time range between the first and last observations) during 2001-2015 are included.  
1016  
1017  
1018  
1019  
1020  
1021  
1022

1023  
1024  
1025  
1026  
1027



1028  
1029 **Figure 10.** Panels (a-d): long-term mean value of surface CO concentration for 2001 – 2015  
1030 from WDCGG sites, and model simulations driven with a priori and a posteriori emissions.  
1031 Panels (e-g): effect of a posteriori emissions, derived by  $\text{abs}(\text{CO}_{\text{aposteriori}} - \text{CO}_{\text{WDCGG}}) -$   
1032  $\text{abs}(\text{CO}_{\text{apriori}} - \text{CO}_{\text{WDCGG}})$ ; blue (red) means the a posteriori emissions improves (degrades) the  
1033 agreement with WDCGG measurements compared to the a priori emissions, while white  
1034 indicates no change from the priori. Only stations with more than 10 year observations (the  
1035 time range between the first and last observations) during 2001-2015 are included.  
1036  
1037  
1038  
1039  
1040  
1041  
1042  
1043

1044  
1045  
1046  
1047  
1048  
1049  
1050  
1051



1052  
1053 **Figure 11.** Long-term trend (annual) of modeled surface and column CO for 2001 – 2015 with  
1054 (a-b) all emission sources are fixed at 2001 level. (c-d) variable anthropogenic emissions; (e-f)  
1055 variable biomass burning emissions; (g-h) variable biogenic VOCs emissions; The variable  
1056 emissions are constrained with MOPITT profile data.